



**Contribution of CNRS  
to the G3P3 project**

## Assessment of the Fluidized Particle-in-tube technology

November 30, 2020

***Contributors:***

*Bataille F.*

*Flamant G.*

*Grange B.*

*Gueguen R.*

*Le Gal A*

Sandia National Laboratories  
Award # DE-FOA-0001697-1503



## Abstract

Phase 1 of G3P3 project includes a comparison of different options of particle solar receivers, namely, the free falling, the centrifugal kiln and the fluidized bed technologies. This report presents some development of the fluidized particle-in-tube technology proposed by CNRS-PROMES. It aims to answer some basic questions that raise after the first experimental demonstrations: are the acceptable particle mass flow rate limited to low values? What is the realistic power and thermal efficiency of a commercial-scale solar receiver based on this technology? What is the LCOE of a commercial plant?

The study of particle flow in a 3m-long and 5cm ID tube indicates that particle mass flow rates up to 0.54 kg/s can be obtained and controlled (it is not the ultimate limit). The associated mean particle volume fraction is approximately 30% in the upward fluidized particle flows. The flow regime is studied using pressure fluctuation measurements along the tube height. Two fluidization regime transitions occur along the tube height. Free bubbling to wall slugging at ~0.70 m above the aeration and wall slugging to axisymmetric slugging at ~1.7 m. The second transition will result in a strong decrease of the wall-to-bed heat transfer coefficient and must be avoided. Fortunately, the position of this transition depends on the operation temperature. It moves upward with a temperature increase. Accounting for this property, 7-8m-long tube is a realistic option for the solar receiver scaling-up.

The thermal efficiency of a 50 MW<sub>th</sub> cavity tubular solar receiver using fluidized particles as HTF is examined as a function the cavity geometry. The absorber is composed of M= 5 panels to house 360 tubes (7 m height) in an arc circle of an angle  $\theta$ . According to design data, the wall temperature is 950°C for particles outlet temperature of 750°C. An either vertical or inclined aperture is assumed, to accommodate the main direction of the reflected solar beam by the heliostats. A thermal efficiency of 90% is feasible but the size of the cavity aperture is too small to allow a high optical efficiency (spillage losses). Nevertheless, 85% thermal efficiency is a realistic target. On this basis, the cost of a multi-tower 100 MW<sub>e</sub> solar power plant is studied.

LCOE estimation indicates that the objective of c\$5/kWh is attainable with the fluidized particle-in-tube technology. However, a more detailed performance evaluation including a yearly production calculation is necessary to confirm this result.

## Table of Content

<b>1. Introduction</b>	p.4
<b>2. Hydrodynamic Study of Fluidized Bed Up flow of Group A Particles in Receiver Tubes</b>	
2.1 Introduction	p.4
2.2 Cold Setup	p.4
2.3 Particles	p.6
2.4 Scientific Background	p.7
2.5 Results	p.12
2.6 Conclusion	p.18
<b>3. Thermal Model of a Commercial-Scale Solar Receiver</b>	
3.1 Introduction	p.19
3.2 Receiver description	p.19
3.3 Thermal model	p.20
3.4 Results	p.25
3.5 Conclusion	p.31
<b>4. Levelized Cost of Electricity (LCOE)</b>	
4.1 Configuration	p.32
4.2 Cost Assumptions	p.33
4.3 LCOE Calculation	p.38
<b>5. Conclusion</b>	p.42
<b>6. Appendix</b>	p.43

## 1. Introduction

This report is the contribution of CNRS-PROMES to the assessment of the fluidized particle-in-tube solar receiver technology in the framework of the G3P3 project. The main objectives defined in common with the G3P3 PI were:

- Demonstrate particle mass flow rate in the range 0.125-0.25 kg/s per tube (50 mm ID) corresponding to a mass flow of 5-10 kg/s in the pilot scale solar receiver.
- Propose solutions to reach the 90% receiver thermal efficiency target and develop a simulation model of the solution.

According to these objectives, section 2 presents the results of CNRS study on particle flow in a single receiver tube and section 3 is dedicated to the modeling of a commercial scale 50MW-solar receiver with the aim to reach an efficiency in the range 80-90%. In addition, we propose in section 4 a LCOE estimation according to the data shared between SNL and DLR.

## 2. Hydrodynamic Study of Fluidized Bed Up flow of Group A Particles in Receiver Tubes

### 2.1. Introduction

This study aims to, firstly demonstrate that the fluidized particle-in-tube technology allows high values of particle mass flux per tube (up to now the particles mass flux was limited to  $110 \text{ kg/m}^2\cdot\text{s}$ )<sup>1</sup> and secondly to examine the gas-particle flow regime in long tubes with respect to their diameter (high aspect ratio).

Understanding the characteristics of the fluidized bed flow in tube with high aspect ratio is critical since the expected formation of axisymmetric slugs will result in a significant decrease of the wall to bed heat transfer. Two flow regime transitions have been identified: from bubbling to wall slugging and from wall slugging to axisymmetric regimes<sup>2</sup>. Axisymmetric slugs significantly hamper the heat transfer because they considerably reduce axial and radial particle mixing, thus hampering particle convective heat transfer. Fortunately, the particle flow characteristics vary strongly with the working temperature. In particular, the slugging transition occurs at higher height at high temperature than at ambient.

### 2.2. Cold Set-Up

The cold mock-up is presented in Figure 1. It is composed of a dispenser, of section  $S_{disp} = 0.571 \pm 0.002 \text{ m}^2$ , in which the particles are uniformly fluidized at a constant air flow rate of fluidization  $\dot{q}_f = 20 \text{ m}^3/\text{h}$  with a porous metal plate distributor. It corresponds to a fluidization velocity  $U_f = 0.972 \pm 0.005 \text{ cm/s}$ , allowing a freely bubbling regime. A glass tube of total height  $H_t = 3.63 \pm 0.002 \text{ m}$  and Internal Diameter (I.D.)  $D_t = 45 \pm 0.05 \text{ mm}$  is plunged into the fluidized bed up to 7 cm above the distributor.

A pressure-control valve controls the absolute pressure in the freeboard of the dispenser, allowing the suspension to flow upward inside the tube by compensating the

---

<sup>1</sup> Le Gal A., Grange B., Tessonnaud M., Perez A., Escape C., Sans J-L., Flamant G (2019). Thermal analysis of fluidized particle flows in a finned tube solar receiver. *Solar Energy* 191, pp. 19–33.

<sup>2</sup> Kong W., Tan T., Baeyens J., Flamant G., Zhang H. (2017), Bubbling and slugging of Geldart group A powders in small diameters columns. *Industrial & Engineering Chemistry Research* 56 (14), pp.4136-4144.

pressure losses of the system<sup>3</sup>. The tube ends with a collector at atmospheric pressure, including a shallow fluidized bed in a freely bubbling regime to facilitate the particles discharge. The difference between the total pressure of the dispenser  $P_{tot}$ , i.e. the sum of the freeboard pressure and the pressure drop through the fluidized bed, and the atmospheric pressure  $P_{atm}$ , is the driving pressure of the system.

A weighting scale is installed at the tube discharge to measure the particle mass flow rate  $\dot{m}_p$ . The storage tank equipped with a rotary valve fed the particle in the dispenser to keep the height of the fluidized bed approximately constant.

A secondary air flow rate called “aeration”,  $q_{ae}$ , is injected in the tube at 0.52 m above the dispenser air distributor with a 3 mm I.D. nozzle to stabilize the particle flow. The conveying tube is equipped with eleven pressure probes spaced of 25 cm of each other, the first probe being located at 18 cm above the aeration. These probes are connected to differential or relative pressure sensors depending on targeted measurements. The sensors and flow meters used have measurement ranges and response times in accordance with the experimental requirements. They are connected to a data acquisition system.

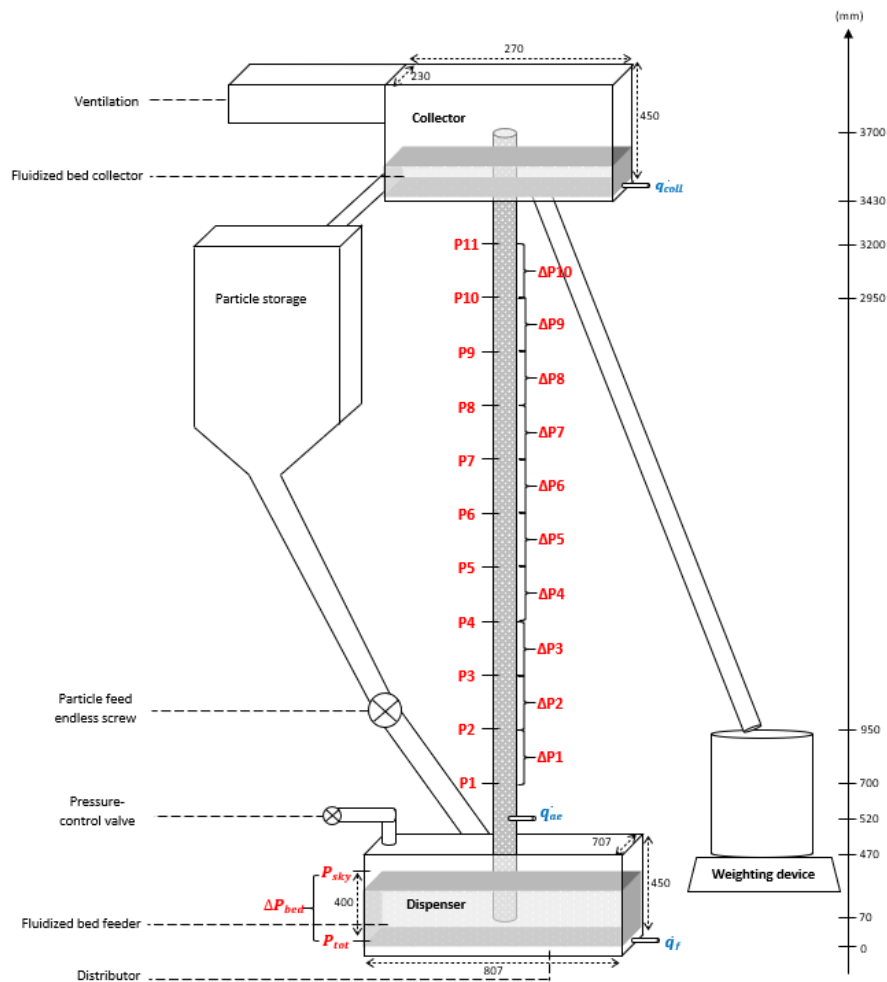


**Figure 1:** Schematic layout of the cold mock-up with instrumentation details.

<sup>3</sup> Zhang H., Kong W., Tan T., Flamant G., Baeyens J. (2017), Experiments support an improved model for particle transport in fluidized beds, Scientific Reports, 7(1), 10178.

The operating parameters of the experimental facility are:

- The aeration air flow rate in the tube  $q_{ae}$ , ranges from 0.51 to 1.41 m<sup>3</sup>/h, corresponding to a superficial air velocity  $U_{ae}$  from 0.09 to 0.25 m/s in the tube.
- The superficial air velocity in the tube  $U_{air}$ , is the sum of the dispenser fluidization and aeration air velocities  $U_f$  and  $U_{ae}$  respectively, and ranges from 0.0094 to 0.246 cm/s.
- The driving pressure of the system  $P_{tot}$ , i.e. the total relative pressure in the dispenser, varies between 20 and 420 mbar. Combined with the aeration injection, it allows the suspension to reach a height in the tube or the flow at a solid mass flux.
- The level of the suspension within the tube  $H_{bed}$ , varies but is limited by the tube height  $H_t = 3.18$  m above the aeration injection.
- The superficial particle mass flux  $G_p$ , i.e. the solid flow rate  $m_p$  divided by the section of the tube  $S_t = 0.0016$  m<sup>2</sup>. It is determined by linear regression of the time-dependent particle mass weight recorded by the weighting scale, and it varies up to 340 kg/m<sup>2</sup>s.

### 2.3. Particles

The particles used are olivine, selected for their thermal and fluidization properties<sup>4</sup>. Firstly, the particle size distribution and the minimum fluidization velocity have been measured.

- The particle size distribution is presented in Figure 2.a. The Sauter diameter  $d_{sv}$  has been estimated at 30 μm. The size spread was calculated as  $\sigma = (d_{90} - d_{10})/2d_{50} = 67.9$  %, with  $d_x$  the diameter corresponding to the x % value on the cumulated distribution graph. These data confirm that particles belong to the group A of the Geldart classification<sup>5</sup>.
- The minimum fluidization velocity  $U_{mf}$  has been measured with the classic pressure drop versus the superficial air velocity method (Figure 2.b). It has been calculated as  $0.40 \pm 0.048$  cm/s.

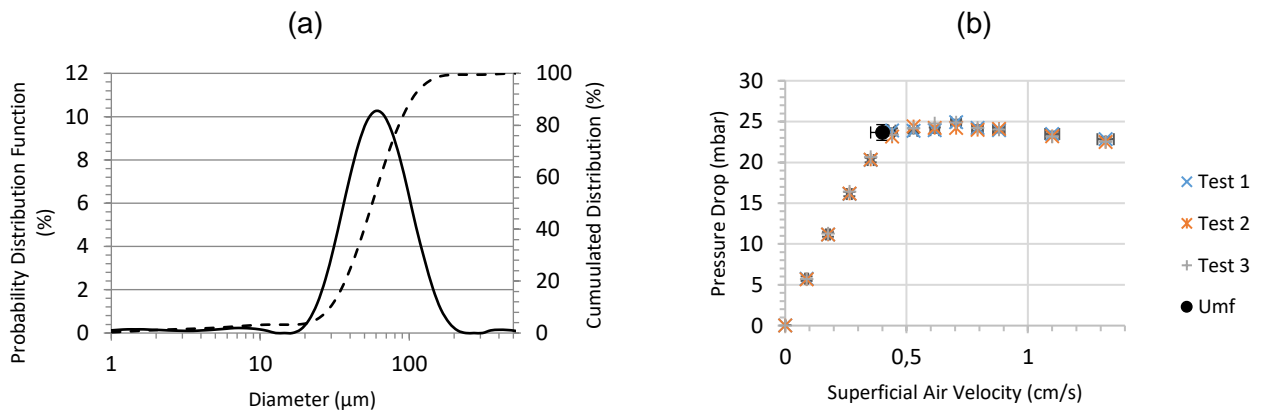


**Figure 2:** a) Particle size distribution, relative (solid curve) and cumulative (dashed curve), and b) Determination of the minimum fluidization velocity by common  $\Delta P$  versus superficial air velocity.

<sup>4</sup> Kang Q., Flamant G., Dewil R., Baeyens J., Zhang H.L., Deng Y.M. (2019), Particles in a circulation loop for solar energy capture and storage, Particuology 43, pp.149-156.

<sup>5</sup> Geldart D. (1973), Types of gas fluidization, Powder Technology 7, pp.285-292.

## 2.4. Scientific Background

### 2.4.1. Solid Volume Fraction Analysis

The dimensionless local solid fraction ( $\alpha$ ) is the proportion of the volume occupied by the particles. It is the opposite of the porosity ( $\varepsilon$ ),  $\alpha = 1 - \varepsilon$ . It is determined from pressure gradient measurements.

In our conditions, the wall friction of the suspension represents only 5-6 % of the pressure drop and can be neglected<sup>6</sup>. Moreover, the pressure drop over a length  $L$  is a sum of three loss contributions<sup>3</sup>: the energy loss to accelerate the particles to the particle velocity,  $\Delta P_{acc} = G_p U_p$ ; the pressure drop exerted by the particles weight,  $\Delta P_p = \alpha_p \rho_p g L$ , and the pressure drop due to particle-to-wall friction,  $\Delta P_{fr} = \frac{3C_D \rho_g H}{4d_{sv} \rho_p} (\rho_p \alpha_p) (U_g - U_p)^2$ , with  $C_D$  the friction coefficient. First, in our experimental ranges, the maximum superficial solid velocity is  $U_p = G_p / \alpha_p \rho_p = 0.31 \text{ m/s}$ . This correspond to  $\Delta P_{acc} \approx 1 \text{ mbar}$  for a driven pressure of 402 mbar, hence completely negligible (nearly 0.26 %, less than pressure fluctuations). Next, for the same test condition, the corresponding friction pressure drop  $\Delta P_{fr} \approx 9 \text{ mbar}$ , i.e. nearly 3 % of the driven pressure (by calculating the  $C_D$  with the method explained by Geldart<sup>7</sup>).

In conclusion, the total friction losses due to particles acceleration and wall friction are around 3 % of the measured pressure drop. This value is in the range of the pressure fluctuations due to the bubbling and/or slugging flow. These losses are hence negligible, and the pressure drop can be expressed in terms of the particles weight only. This leads to the average local solid volume fraction in a volume between two pressure probes (Eq. 1), at the average height  $\bar{h}_i = \frac{h_{i+1} + h_i}{2}$ , and with  $\Delta h_i = h_{i+1} - h_i = 25 \pm 0.1 \text{ cm}$  the distance between two probes.

$$\alpha_i(\bar{h}_i) = \frac{\Delta P_i}{(\rho_p - \rho_g) g \Delta h_i} \quad (1)$$

In equation 1,  $\Delta P_i$  is the averaged value of the  $i^{\text{th}}$  differential signal pressure (an example is shown in Figure 3). An uncertainty is associated with the solid fraction measurement, due to the pressure fluctuations (i.e. the fluidization regime). It is calculated as the standard deviation of the signal added to the sensor measurement error (0.05 mbar for the sensors used, negligible in comparison with the absolute value of the pressure fluctuations).

---

<sup>6</sup> Srivastava A. and Sundaresan S. (2002), Role of wall friction in fluidization and standpipe flow, Powder technology 124, pp.45-54.

<sup>7</sup> Geldart D. (1986), Gas Fluidization Technology, Chap 6. Particle Entrainment and Carryover, pp.123-154.

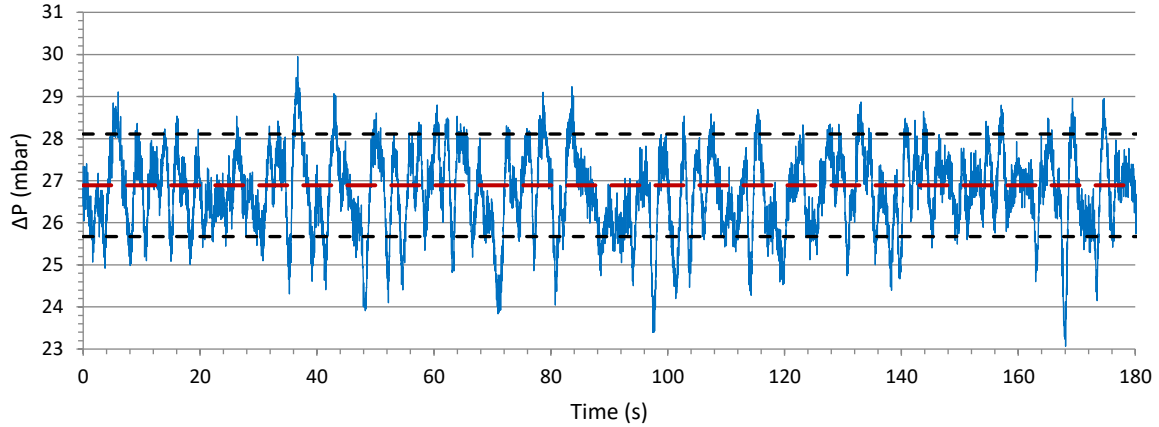


**Figure 3:** Example of a differential pressure during a test. The dashed red line indicates the average value, and the block one corresponds to the associated standard deviation.

The overall solid fraction is also calculated as the average of the ten local fractions,  $\alpha_h = \frac{1}{10} \sum_{i=1}^{10} \alpha_i$ . The associated uncertainty,  $\Delta\alpha_h = \frac{1}{10} \sum_{i=1}^{10} \Delta\alpha_i$ , with  $\Delta\alpha_i$  the uncertainty calculated from equation 1.

#### 2.4.2. Flow Structure

The pressure probes are also connected to relative pressure sensors, in order to analyze the fluctuations of the signals by both temporal and frequency methods.

##### 2.4.2.1. The Cross-Correlation

Due to the flow regimes, i.e. bubbling, slugging or even turbulent flow, the relative pressure signals have similar shapes: a succession of upper and lower peaks. Actually, the passage of a void perturbation (i.e. a bubble or a slug) in front of a pressure probe will cause an upper peak on the corresponding pressure signal, and the lower peak will be caused by the wake of the bubble<sup>8,9,10</sup>. Both an upper and lower peaks above and below the average pressure at the sampling position are considered in literature as representative of slugs. Random upper/lower peaks, but not crossing the average pressure values, are considered to be due to freely rising and coalescing bubbles.

Thus, when considering two pressure signals at successive positions, as presented in Figure 4, it is possible to easily identify slugs by spaced upper and lower peaks, and observe that there is a temporal shift for characteristic peaks on the height. This shift is due to the moving of the perturbation over the tube, and can be used to determine the velocity of the perturbation knowing the distance between the recorded signals.

<sup>8</sup> Fan L.T., Ho T.C., Walawender W.P. (1983), Measurements of the rise velocities of bubbles, slugs and pressure waves in a gas-solid fluidized bed using pressure fluctuation signals, American Institute of Chemical Engineers Journal 29, pp.33-39.

<sup>9</sup> Lee G.S., Kim S.D. (1989), Rise velocities of slugs and voids in slugging and turbulent fluidized beds, Korean Journal of Chemical Engineering 6, pp.15-22.

<sup>10</sup> Johnsson F., Zijerveld R.C., Schouten J.C., van den Bleek C.M., Leckner B. (2000), Characterization of fluidization regimes by time-series analysis of pressure fluctuations, International Journal of Multiphase Flow 26, pp.663-715.

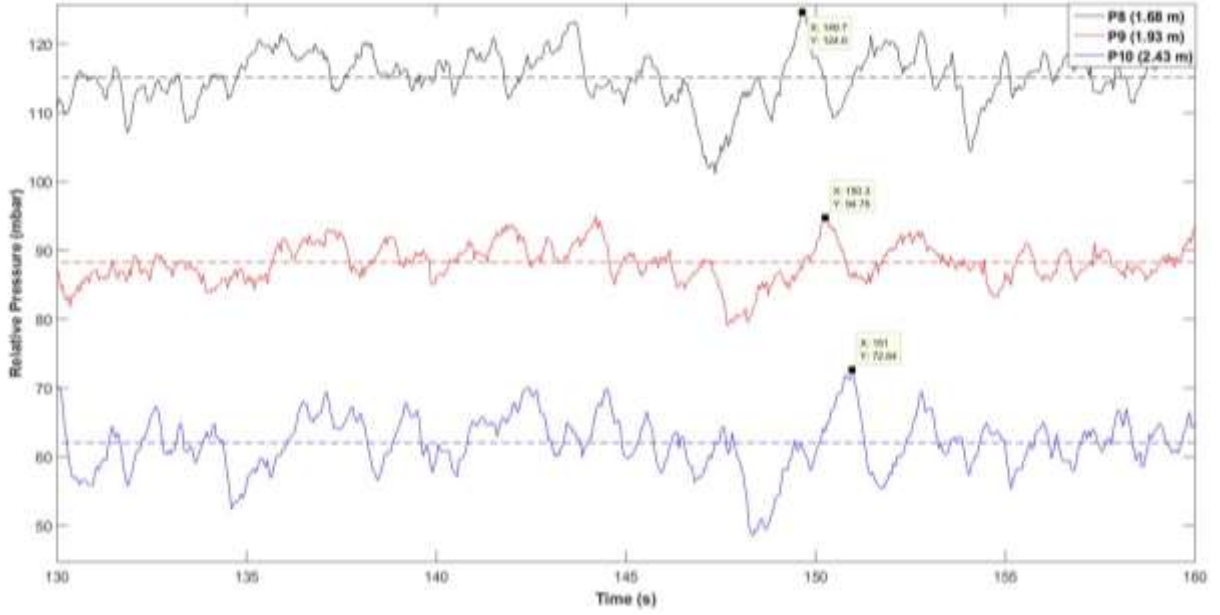


**Figure 4:** Three relative pressure fluctuations measured at various height above the aeration, with the average value of each signal in dashed lines, for a test with a superficial excess air velocity  $U_{air} - U_{mf}$  of  $0.182 \pm 0.005$  m/s and a solid mass flux  $G_p$  of  $15.3 \pm 0.5$  kg/m<sup>2</sup>s.

In Figure 4, one can identify three peaks for the same perturbation (slug) at three successive heights, corresponding to three acquisition times: 149.7, 150.3 and 151 seconds respectively. Accounting for the distance between the two pressure probes, i.e. 25 cm, the upward slug velocity is 0.417 m/s between 0.68 and 1.93 m above the aeration nozzle, and 0.357 m/s between 1.93 and 2.43 m.

The previous explanation is a graphical approach. From the mathematic point of view, the pressure signals at two successive positions are characterized by two functions  $x(y)$  and  $y(t)$ , with  $x$  the lower position. The cross-correlation signal  $R_{xy}$  determines how much  $y$  must be shifted along the time axis to make it nearly identical to  $x$  (Eq. 2.a). When the upper and lower peaks are aligned, their contributions to the integral are maximum. Thus the value of  $x * y$  is maximized when the functions match, hence identifying the corresponding time lag  $\tau$ .

$$R_{xy}(\tau) = \frac{1}{N} \int x(t) * y(t + \tau) dt \quad (2.a)$$

$$R_{xy}(k) = \frac{1}{N - k} \sum_{n=1}^{N-k} x(t) y(t + k) \quad (2.b)$$

During experiments, as  $x$  and  $y$  are discrete signals, the formula needs discrete approach, and the cross-correlation over  $N$  points is calculated for various time lags  $\tau$ , which correspond to numerical lags  $k = \tau * f_{acq}$ , with  $f_{acq}$  the acquisition frequency (Eq. 2.b). The cross-correlation function is then maximum for the time lag  $\tau_m$ . Knowing the distance between the two successive positions along the tube  $\Delta h$ , this time lag is linked to the upward slug velocity, averaged over the acquisition time at the examined height  $\bar{h}_i$ ,  $U_s(\bar{h}_i) = \Delta h / \tau(\bar{h}_i)$ . Figure 5 shows the cross-correlation functions calculated for the example presented above in

Figure 4,  $R_{8,9}$  and  $R_{9,10}$  respectively. The time lags  $\tau_m$  are identified as 0.6 and 0.5 seconds respectively, corresponding to slug velocities for this test at 0.417 and 0.500 m/s.

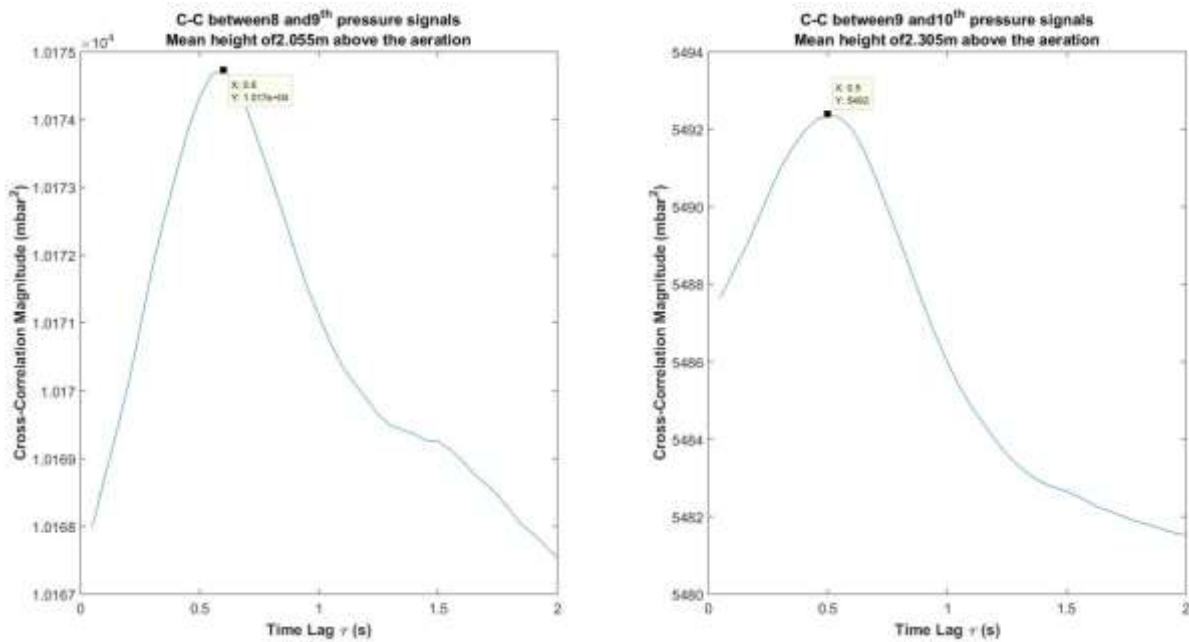


**Figure 5:** Calculated cross-correlation of the pressure signals shown in Figure 4.

#### 2.4.2.2. The Coherence Analysis

The frequency of a void perturbation, i.e. the number of bubble or slug moving in front of a pressure probe per second, can be detected by analyzing the fluctuations of a temporal relative pressure signal. It consists in operating in the frequency domain by applying a Fourier Transform of the signal to calculate its power spectrum, which describes the distribution of power into frequency components. The dominant frequency of this new signal in the frequency domain, i.e. the frequency corresponding to the maximum power (or magnitude) of the signal, is representative of the perturbation.

In Figure 4, on the basis of the number of characteristic upper or lower peaks during the test duration, the slug frequency is around 0.57 Hz at this height.

A pressure time signal  $x(t)$  can be decomposed in  $M$  groups of  $N$  points. Then, the power spectral density (PSD) function of the  $i^{\text{th}}$  signal is defined by Equation 3.a, where the brackets denote the ensemble average over the  $M$  groups, and  $F_i(f)$  is the Fourier transform of the signal, calculated with a Fast Fourier Transform algorithm (FFT). In complex flows, there are many noisy frequencies on the PSD function, corresponding to pressure waves associated with the experimental device, or to the small bubbles in the dispenser. To overcome these noisy frequencies, the signal can be decomposed in  $M$  groups, in order to smooth the signal and thus extract the representative frequencies.

Another solution is to use the coherence analysis method<sup>11</sup>. According to previous authors, “the amplitude of the pressure waves decrease linearly with distance from the point

<sup>11</sup> Van der Schaaf J., Schouten J.C., Johnsson F., van den Bleek C.M. (2002), Non-intrusive determination of bubble and slug length scales in fluidized beds by decomposition of the power spectral density of pressure time series, International Journal of Multiphase Flow 28, pp.865-880.

of origin to the bed surface but do not decrease in the downward direction. Thus, the pressure waves are also measured in the plenum of the fluidized bed and will thus be coherent with the in-bed positions.” These frequencies can be deleted by calculating the cross power spectral density (CPSD) function between the  $i^{\text{th}}$  pressure signal and a chosen reference, denoted by the “0” subscript (Eq. 3.b). This reference has to be measured at a lower position than the studied signal.

$$\phi_{ii}(f) = \frac{1}{N} \langle F_i(f) F_i^*(f) \rangle \quad (3.a)$$

$$\phi_{i0}(f) = \frac{1}{N} \langle F_i(f) F_0^*(f) \rangle \quad (3.b)$$

If the time series are coherent for one frequency, the CPSD function is thus maximum, similar to the cross-correlation function presented in the previous section. To normalize this quantity, the authors define the coherence term,  $\gamma_{i0}^2$  (Eq. 4).

$$\gamma_{i0}^2(f) = \frac{\phi_{i0}(f) \phi_{i0}^*(f)}{\phi_{ii}(f) \phi_{00}(f)} \quad (4)$$

Then, the coherent part of the  $i^{\text{th}}$  signal  $COP_{i0}$  is representative of the fast pressure fluctuations associated to the small fast bubbles formed in the dispenser and measured at the reference signal (Eq. 5.a), while the incoherent part  $IOP_{i0}$  reflects the local phenomena, i.e. bubbles and slugs (Eq. 5.b). The dominant frequency of this new signal hence represents the bubble or slug frequency at the sensor height.

$$COP_{i0}(f) = \gamma_{i0}^2(f) * \phi_{ii}(f) \quad (5.a)$$

$$IOP_{i0}(f) = (1 - \gamma_{i0}^2(f)) * \phi_{ii}(f) \quad (5.b)$$

Figure 6 shows the spectrum calculated with the coherence analysis with the  $P1$  sensor as the reference, for the example presented in Figure 4, i.e.  $IOP_{8,1}$ ,  $IOP_{9,1}$  and  $IOP_{10,1}$  respectively. Here, the signals are decomposed in 4 groups of 1024 points each, with an acquisition frequency of 20 Hz. The dominant frequencies are identified at 0.31 Hz for the three signals.

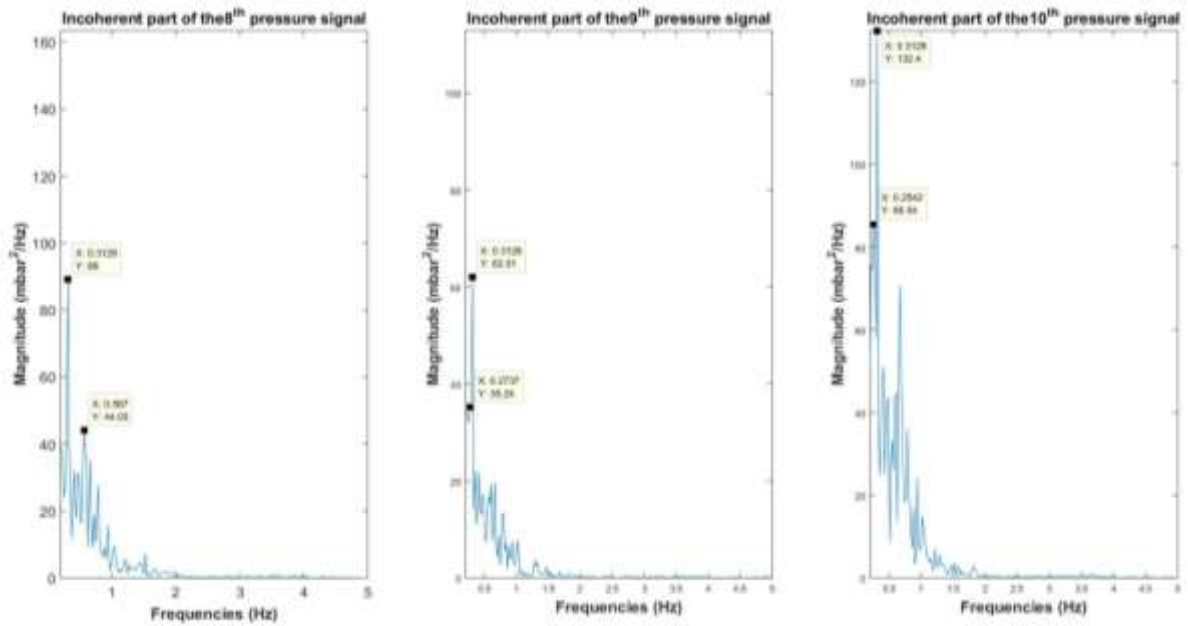


**Figure 6:** Calculated incoherence spectrum of the pressure signals shown in Figure 4.

## 2.5. Results

The following section presents the results of 34 tests without particles circulation and 60 tests with circulation, in order to determine the influence of the experimental parameters on the suspension behavior and its structure.

### 2.5.1. Solid mass flux

The domain of variation of the experimental parameters with particles circulation is presented in Table 1, separated in low and high solid mass flow rates  $\dot{m}_p$ , with their corresponding particles mass fluxes  $G_p$ , driving pressures  $P_{tot}$  and aeration velocities  $U_{ae}$ .

**Table 1.** Domain of variation of the experimental parameters.

		Low mass flow rates	High mass flow rates
<b>Solid mass flux <math>G_p</math> (kg/m<sup>2</sup>s)</b>		0 – 200	200 – 340
<b>Solid mass flow rate <math>\dot{m}_p</math></b>	<b>(kg/h)</b>	0 – 1144	1144 – 1950
	<b>(kg/s)</b>	0 – 0.318	0.318 – 0.542
<b>Driving pressure <math>P_{tot}</math> (mbar)</b>		338 – 410	370 – 410
<b>Superficial aeration velocity <math>U_{ae}</math> (m/s)</b>		0.088 – 0.246	0.132 – 0.246

To maintain a good stability of the flow, the aeration airflow rate must be set above a threshold value, in particular for high solid mass fluxes. The maximum solid flux obtained is 340 kg/m<sup>2</sup>s, i.e. nearly 2 tons/h. This is not the maximum solid flux of the system, because we are in practice limited by the storage tank volume (see Figure 1).

## 2.5.2. Solid Volume Fraction

### 2.5.2.1. Overall Volume Fraction

Firstly, without particle circulation (no-circulation case), the solid volume fraction is determined as a function of the bed height, expressed above the aeration nozzle, with the aeration velocity  $U_{ae}$  as a parameter (Figure 7.a).  $H_{bed}$  has a small influence on the global volume fraction,  $\alpha_h$ . However, the same figure illustrates  $\alpha_h$  varies significantly with the aeration air flow rate. With particle circulation,  $\alpha_h$  is measured with respect to the particle mass flux  $G_p$  (Figure 7.b). Similar conclusion as without particle circulation can be drawn. In these two figures, the error bars are due to the pressure fluctuations, and thus reflect the flow regime. This is discussed later in this report.

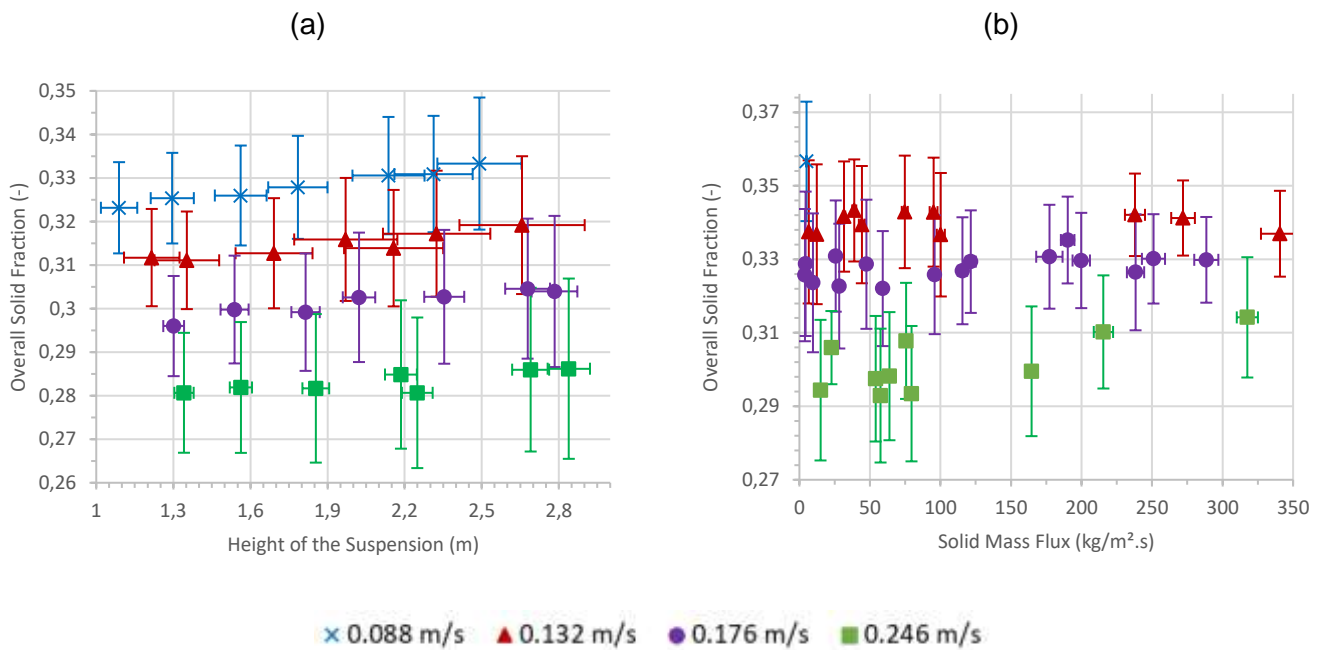


**Figure 7:** Evolution of the overall solid volume fraction versus a) the height reached by the suspension and b) the solid mass flux, for four aeration flow rates.

The influence of the aeration flow rate on  $\alpha_h$  is shown in Figure 8, in terms of the superficial excess air velocity in the tube,  $U_{air} - U_{mf}$ . The different points for each velocity correspond to the various height of the suspension or solid mass flux. To avoid overloading, the error bars are represented with dashed lines corresponding to the maximum and minimum deviations from the average values.

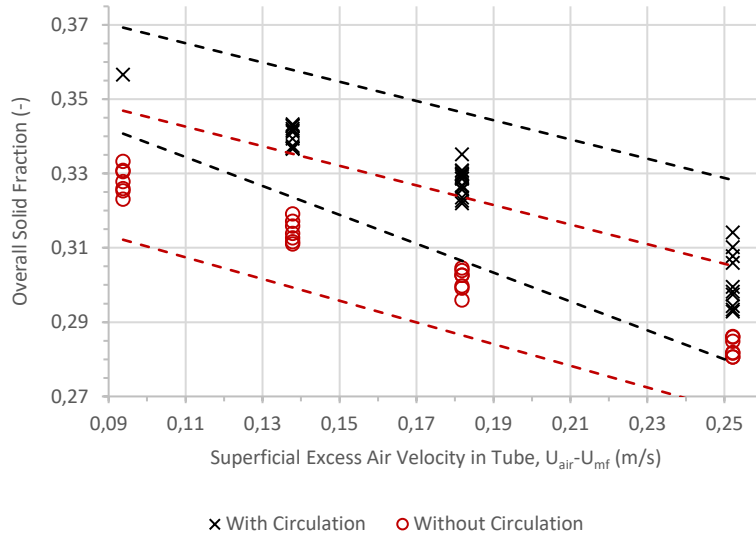


**Figure 8:** Influence of the superficial air velocity on the overall solid fraction, with and without circulation.

A linear variation of  $\alpha_h$  with the air velocity can be observed in agreement with Boissiere *et al.*<sup>12</sup>. Therefore, the air velocity is the dominant experimental parameter affecting the particle volume fraction. This behavior was expected, because an increase of the aeration flow rate results in an increase of the quantity of air injected in the tube, thus the bed porosity.

Moreover, the suspension is denser with particle circulation than without, irrespective of the solid flux or the height of the suspension.

There is only one point shown at the lowest aeration flow rate with particles circulation because the solid flow was unstable. It has been identified that a minimum aeration velocity of 0.132 m/s was required to generate a stable particles flow. The results presented below are thus only in the stability domain.

### 2.5.3. Flow Hydrodynamic

The fluctuations of the relative pressure signals are treated with the methods explained in section 2.3.2.

#### 2.5.3.1. Coherence Analysis and Frequencies

The coherence analysis has been applied with the first sensor *P1* as the reference, to determine relevant frequencies. The frequencies shown in Figure 9 are the dominant frequencies after the coherence analysis, i.e. the frequencies which correspond to the maximum magnitude of the spectrum.

<sup>12</sup> Boissière B., Ansart R., Gauthier D., Flamant G., Hemati M. (2015), Experimental hydrodynamic study of gas-particle dense suspension upward flow for applications as new heat transfer and storage fluid, The Canadian Journal of Chemical Engineering 93, pp.317-330.

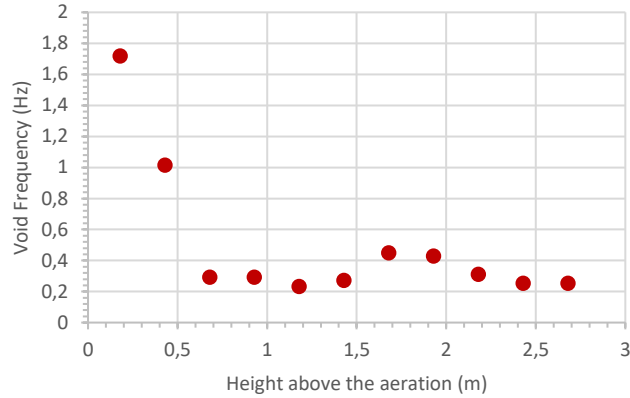


**Figure 9:** Evolution of the void frequency versus tube height measured with the coherence method, for a test with a superficial excess air velocity of  $0.182 \pm 0.005$  m/s and a particle mass flux of  $22.66 \pm 0.68$  kg/m<sup>2</sup>s.

Two flow transitions appear in Figure 9. The first one is clearly identified as a transition between the bubbling regime (at the bottom of the tube) and the wall slugging regime. The transition is detected around 0.70 m above the aeration nozzle. The second transition is observed at approximately 1.70 m where a change of the slug frequency occurs. In agreement with observations, this change is attributed to a transition between wall slugging and axisymmetric slugging regimes (see 2.5.3.2).

It is difficult to identify a mean value of the frequency for one test. Actually, because of the sensibility of the post-treatment, even a slight instability of the flow can cause a strong noise on the spectrum. In such cases, the second dominant frequency (in terms of magnitude) of the signal is useful to derive the relevant frequency of the perturbations.

### 2.5.3.2. Cross-Correlation and Velocities

Due to the lack of significant pressure fluctuations associated to the bubbles in the bed, the cross-correlation method can be applied only to the measurement of the slug velocities and their evolution with the height, as shown in Figure 10.

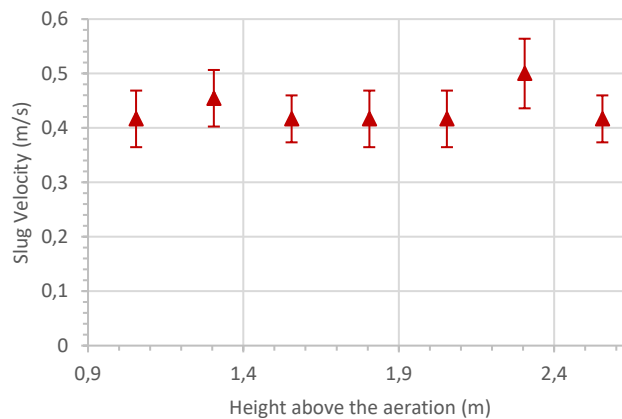


**Figure 10:** Evolution of the slug frequency versus the height measured with the cross-correlation method, for a test with an superficial excess air velocity of  $0.182 \pm 0.005$  m/s and a particle mass flux of  $22.66 \pm 0.68$  kg/m<sup>2</sup>s.

The value of the rising slug velocity associated to this test,  $U_s$ , is taken as the average of the significant data. It is then possible to represent the evolution of  $U_s$  versus the solid mass flux, for different aeration flow rates (Figure 11). Without particle circulation, the height of the suspension has a slight influence on the slug velocity. Thus the corresponding points are represented in Figure 11 at the value  $G_p = 0$ .

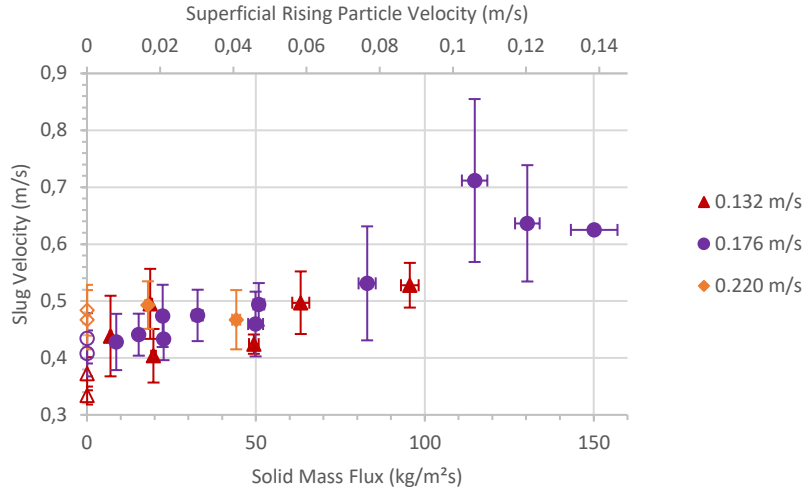


**Figure 10:** Evolution of the slug velocity versus the solid mass flux, for the aeration velocity  $U_{ae}$  as a parameter.

The results are in good agreement with the two-phases theory of fluidization, where the slug velocity is expressed with  $U_s = (U_{air} - U_{mf}) + U_p + k\sqrt{gD_t}$ , with  $k = 0.35$  or  $0.7$  depending on the slugging regime axisymmetric or wall respectively<sup>2</sup> and  $U_p = \frac{G_p}{\alpha\rho_p}$ . The measured slug velocities correspond to the axisymmetric regime.

### 2.5.3.3. Transition Between Fluidization Regimes – Additional data

The study of the pressure fluctuations allows identifying fluidization regime transitions. First, the integral of the incoherent part of the signal being relative to bubbles and slugs, it is directly related to the bubbles/slugs diameter,  $D_b$  (Eq. 6)<sup>13</sup>.

$$\sqrt{\int_{\infty} IOP_{i0}(f)df} \propto D_b \alpha_h \rho_p g \quad (6)$$

As an example, the evolution of this quantity is presented in Figure 12, for the same test as previously. The first transition (bubbling to wall slugging transition) at around 0.70 m above the aeration can be identified by a sudden increase of  $D_b$ , while another change around 1.70 m is correlated with the second transition (wall slugging to axisymmetric slugging).

<sup>13</sup> Van der Schaaf J., Schouten J.C., Johnsson F., van den Bleek C.M. (2002), Non-intrusive determination of bubble and slug length scales in fluidized beds by decomposition of the power spectral density of pressure time series, International Journal of Multiphase Flow 28, pp.865-880.

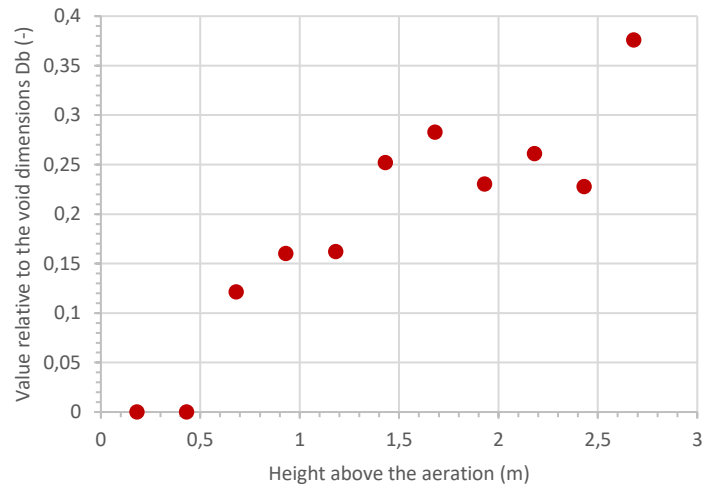


**Figure 12:** Evolution of the relative void dimensions,  $D_b$ , versus the height measured, for a test with an superficial excess air velocity of  $0.182 \pm 0.005$  m/s and a particle mass flux of  $22.66 \pm 0.68$  kg/m<sup>2</sup>s.

The evolution of the amplitude of the pressure fluctuations is also a pertinent indicator of the flow regimes. It is defined as the ratio between the standard deviation of the time-dependent pressure signal and its average value,  $\sigma(P)/P_{moy}$  (Figure 13). The two flow transitions are associated with an increase of the magnitude of the pressure fluctuations, especially the transition between wall slugs and axisymmetric slugs, where the fluctuations increase dramatically.

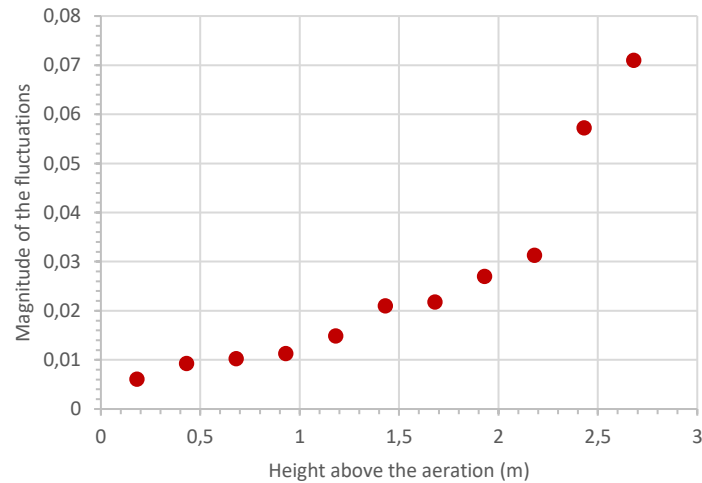


**Figure 13:** Evolution of the magnitude of the pressure fluctuations versus the height measured, for a test with a superficial excess air velocity of  $0.182 \pm 0.005$  m/s and a particle mass flux of  $22.66 \pm 0.68$  kg/m<sup>2</sup>s.

The two previous methods combined with the cross-correlation and the coherence analysis, corroborate the existence of two flow transitions in the tube at approximately 0.70 m and 1.70 m above the aeration nozzle respectively. The location of these transition is

independent of the aeration flow rate or on the particle mass flux, as illustrated in Figure 14, provided the uncertainty due to the distance between the pressure probe (0.25 m) that explains the experimental points in the bubbling domain below the 0.7 m. This observation is in good agreement with Kong *et al.*<sup>14</sup> and allows to complete their diagram with a transition in the slugging zone.

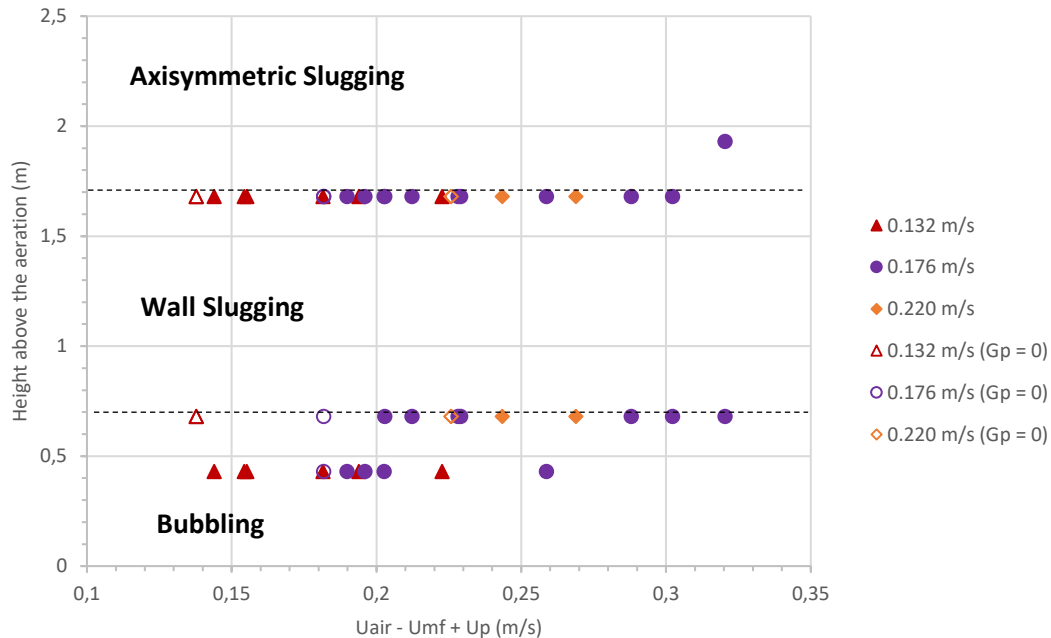


**Figure 14:** Diagram of the different flow regimes in the tube above the aeration nozzle.

## 2.6. Conclusion

This study with a cold mockup demonstrated that the fluidized particle-in-tube solar receiver can be operated with high values of particle mass flux, up to 340 kg/m<sup>2</sup>s, without chocking. The mean particle volume fraction is approximately 30 % (28-34 %) and varies with the aeration mass flow rate. Two transitions of fluidization regime occur along the tube height. Free bubbling to wall slugging at ~0.70 m above the aeration and wall slugging to axisymmetric slugging at ~1.7 m. The second transition will result in a strong decrease of the wall-to-bed heat transfer coefficient and must be avoided. Fortunately, the position of this transition depends on the operation temperature. It moves upward with a temperature increase<sup>14</sup>. Nevertheless, whatever the temperature, there exists a limited length of the tube that was estimated to 7-8 m at 800°C. This constraint leads to a limited size and power of a commercial solar receiver of approximately 50 MW<sub>th</sub>. The thermal efficiency of such a receiver is modeled in the next section.

<sup>14</sup> Kong W., Tan T., Baeyens J., Flamant G., Zhang H. (2017), Bubbling and slugging of Geldart group A powders in small diameters columns, *Industrial & Engineering Chemistry Research* 56 (14), pp.4136-4144.

### 3. Thermal Model of a Commercial-Scale Solar Receiver

#### 3.1. Introduction

This section presents a simplified thermal model of a commercial size solar receiver based on the fluidized particle-in-tube concept accounting for the limited height of the tubes (as introduced in the previous section). The results have been published in [Gueguen, R.; Grange, B.; Bataille, F.; Mer, S.; Flamant, G. *Shaping High Efficiency, High Temperature Cavity Tubular Solar Central Receivers. Energies* 2020, 13, 4803. DOI : <https://doi.org/10.3390/en13184803>].

#### 3.2. Receiver Description

The design of the receiver results from a trade-off between the necessity to correctly direct the solar flux from the heliostats field to the absorber and thus open the cavity, and the thermal losses limitation, which tends to limit the cavity aperture dimensions. For a solar tower situated in the Northern Hemisphere, the absorber in the top of the tower is oriented north-facing, and have a semi-circular form. It is composed of 7m-long vertical tubes, in which the fluidized particles are circulating to extract the solar power. They are considered as flat receiving walls, placed in the cavity with the shape of an arc of a circle (Figure 15). During operation, part of the solar power is extracted by the particles flowing inside the tubes (useful power) and part is dissipated by thermal losses. These losses are shown in the figure. They are composed of convection, conduction and radiation losses and are detailed in the following section.

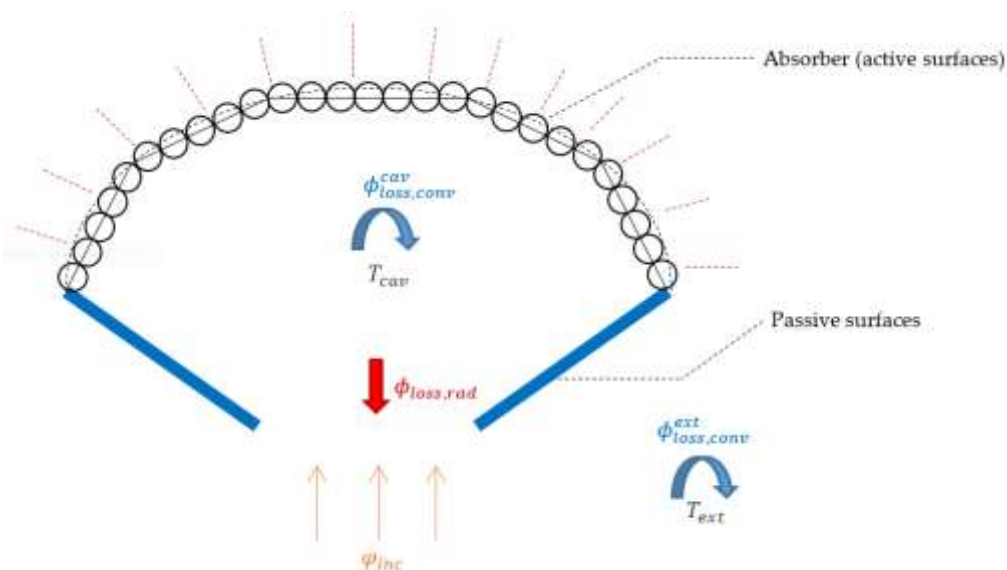


**Figure 15:** Schematic view of the receiver's cavity studied, with the different thermal fluxes. Red dashed lines indicate thermally insulated walls.

The space between the tubes being very small, it is assumed to be zero to focus the study on the influence of the cavity's geometry. Then, the space between the tubes and the rear face of the cavity being very small too, the convection with the air will be low and not be established, thus the spaced is considered null and the insulation of the rear faces is considered perfect. The passive walls are made of insulating and reflective material (in blue on Figure 15) to redirect a part of the radiation towards the absorber. The conduction through

these surfaces is taken into account, because it results in an external temperature (outside of the cavity) above the ambient temperature, and then another kind of convection losses. Finally, the cavity is opened to irradiate the absorber. The radiation losses are the sum of the fluxes that come out of the cavity.

The materials selected for this study are common materials used in commercial solar plant: tubes are made of Inconel 601<sup>15</sup> covered with Pyromark 2500©<sup>16</sup>. Reflective surfaces are considered in Scuttherm<sup>17</sup>. Table 2 lists the selected materials properties.

**Table 2.** Properties of the materials used.

	Absorptivity $\alpha^{sol}$	Reflectivity $r^{sol}$	$\alpha^{IR}$	$r^{IR}$	Emissivity $\epsilon^{IR}$	Density $\rho$ (kg/m <sup>3</sup> )	Thermal Conductivity $\lambda$ (W/mK)
Absorbent Surfaces	0.9	0.1	0.85	0.15	0.85	8110	26.1
Reflective Surfaces	0.22	0.78	0.95	0.05	0.95	315	0.1

Concerning the particles, selected material is olivine, which physical properties are presented in the previous section. An average specific heat is calculated for the study, based on the range of the particle temperature variation in the receiver,  $C_{p,olivine} = 1.3$  kJ/kgK.

### 3.3. Thermal Model

#### 3.3.1. Geometry Parametrization

The receiver is parametrized to study its influence on the thermal performances.

##### 3.3.1.1. The absorber

As mentioned previously, the absorber shape is a circular arc. This arc is discretized into  $M$  panels of  $N$  tubes each (Figure 16). Mathematically, an arc of a circle is defined by a radius of curvature  $r$  and an arc angle  $\theta$ , or else by the chord  $c$  and the arrow  $f$  of its two ends.

<sup>15</sup> Alloy Wire International, Inconel 601. Available online: [www.alloywire.fr/products/inconel-601](http://www.alloywire.fr/products/inconel-601) (accessed on 11 September 2020).

<sup>16</sup> Ho, C.K.; Mahoney, A.R.; Ambrosini, A.; Bencomo, M.; Hall, A.; Lambert, T.N. Characterization of Pyromark 2500 paint for high-temperature solar receivers. *J. Sol. Energy Eng.* 2014, 136, 014502, doi:10.1115/1.4024031.

<sup>17</sup> Refractaris R, Properties of Scuttherm. Available online: [www.refractaris.com](http://www.refractaris.com) (accessed on 11 September 2020).

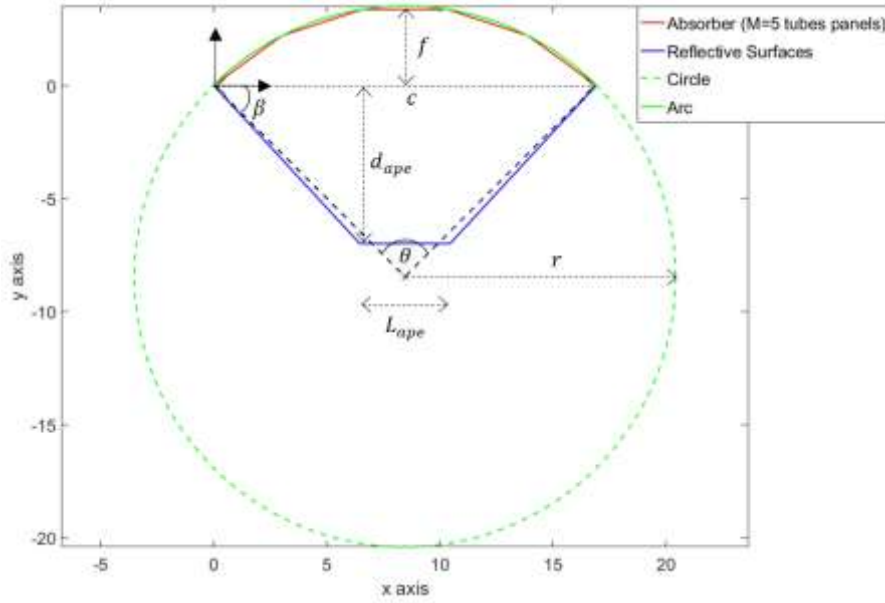


**Figure 16:** Definition of the geometrical parameters with a top view of a section  $(x,y)$  of the receiver.

The left end of the absorber defines the origin of the Cartesian coordinates. The  $M + 1$  arc vertices are calculated from the arc center point of coordinates  $\left(\frac{c}{2}, -(r - f)\right)$ . As the number of tubes is fixed to meet the power objective of the receiver (see following section), the radius of the arc corresponds to the minimum value to insert all the  $N_t$  tubes in the  $M$  panels (Eq. 7), with  $D_t$  the internal tubes diameter of 50 mm and  $e_t$  their thickness of 2 mm. The absorber geometry is then varied changing the two parameters  $M$  and  $\theta$ .

$$r = \frac{N_t(D_t + 2e_t)}{M\sqrt{2\left(1 - \cos\left(\frac{\theta}{M}\right)\right)}} \quad (7)$$

### 3.3.1.2. The aperture

The aperture of the cavity is considered as a rectangle of length  $L_{ape}$  and height  $H_{ape}$ . It is situated at a distance  $d_{ape}$  from the absorber's origin. Even if the absorber's tubes are vertical, the aperture is tilted by an angle  $\alpha$  with the vertical to facilitate the irradiation of the absorber from the heliostats field. Figure 17 shows a sectional side-view of the cavity, with the derived new geometrical quantities ( $H_\alpha$  and  $d_\alpha$ ) and the aperture in black, the lateral panels in blue and the absorber tubes in red. The aperture vertices are then known, and its geometry is defined by four parameters:  $L_{ape}$ ,  $H_{ape}$ ,  $d_{ape}$ ,  $\alpha$ .

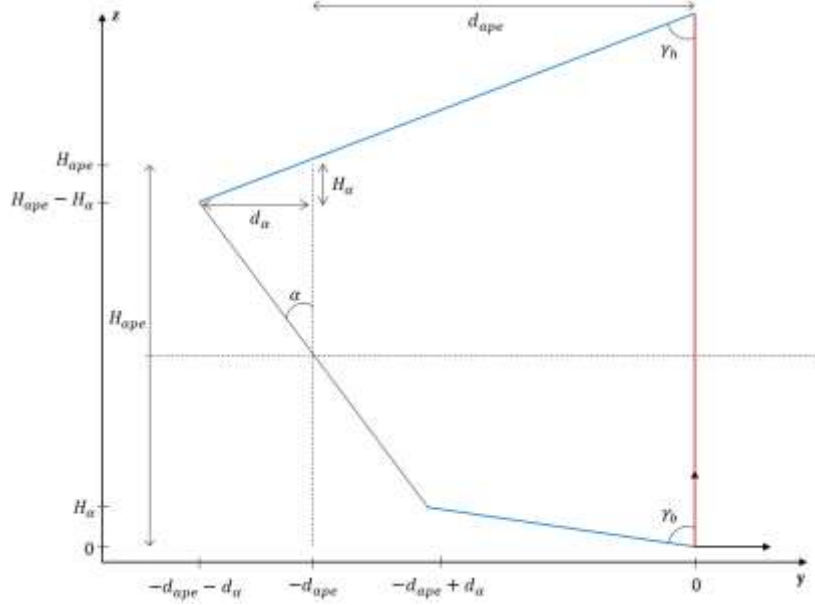


**Figure 17:** Side view of a section ( $y,z$ ) of the receiver, showing the aperture tilt angle  $\alpha$  and the geometrical parameters associated with it.

The surfaces and vertices of the absorber and the aperture are numbered and set in a Matlab program.

### 3.3.2. Preliminary Calculations

In this simplified thermal model, two preliminary calculations are needed to set some parameters values.

#### 3.3.2.1. Tubes Number

The number of tubes is calculated as a function of the extracted power objective. This power can be expressed with a thermal balance on the particles in the tubes (Eq. 8). Here,  $\dot{m}_p$  is the particles mass flow rates per tube, and  $T_{part}^{in}$  and  $T_{part}^{out}$  are the temperatures of the particles at the inlet and the outlet of the tubes, respectively, fixed at 550°C and 750°C for the study.

$$\phi_{abs} = \dot{m}_p N_t C_{p,olivine} (T_{part}^{out} - T_{part}^{in}) \quad (8)$$

Another method to express the power absorbed by the particles is based on the targeted efficiency  $\eta_{rec}$  of 85 % and the power of the receiver  $P_{rec}$  fixed at 50 MW<sub>th</sub>:  $\phi_{abs} = \eta_{rec} P_{rec}$ . Equalizing the two formulations, and considering a particles mass flux  $G_p = \dot{m}_p / (\pi D_t^2 / 4)$  of 250 kg/m<sup>2</sup>s, one obtains a total number of tubes  $N_t$  of approximately 360.

#### 3.3.2.2. Incident Solar Flux

The second parameters to set is the incident concentrated solar flux. It has to be high to fulfill the extracted power objective, but low enough to avoid high wall temperatures, leading to hot spot and then to the absorber damage. First, the extracted power is here expressed for a single tube in terms of the wall-to-fluidized bed heat transfer coefficient,  $h_{t,part}$ , estimated at

1200 W/m<sup>2</sup>K based on previous experimental data<sup>18</sup> (Eq. 9.a). This coefficient is based on the mean logarithmic temperature difference in the tube  $\Delta T_{lm,part}$  and on the exchange surface corresponding to the irradiated part of the tube,  $A_t = \frac{\pi}{2} D_t H_t$ . To simplify, no temperature variation along the tube wall is considered, which simplifies the formulation of  $\Delta T_{lm,part}$  (Eq. 9.b).

$$\phi_{abs} = h_{t,part} A_t \Delta T_{lm,part} \quad (9.a)$$

$$\Delta T_{lm,part} = \frac{(T_{wall}^{in} - T_{part}^{in}) - (T_{wall}^{out} - T_{part}^{out})}{\ln\left(\frac{T_{wall}^{in} - T_{part}^{in}}{T_{wall}^{out} - T_{part}^{out}}\right)} \approx \frac{T_{part}^{out} - T_{part}^{in}}{\ln\left(\frac{T_{wall} - T_{part}^{in}}{T_{wall} - T_{part}^{out}}\right)} \quad (9.b)$$

Equalizing this formulation with the extracted power based on the targeted efficiency on a single tube,  $\phi_{abs} = \eta_{rec} A_t \phi_{inc}$ , leads to the expression of the tube wall temperature as a function of the incident solar flux (Eq. 10).

$$T_{wall} = \frac{T_{part}^{out} * e^x - T_{part}^{in}}{e^x - 1}, \text{ with } x = \frac{h_{t,part} (T_{part}^{out} - T_{part}^{in})}{\eta_{rec} \phi_{inc}} \quad (10)$$

The thermomechanical stress of Inconel 601 imposes a wall temperature limit of 1000°C, reached for a 480 kW/m<sup>2</sup> solar flux. For security, the maximal solar flux density is set to 400 kW/m<sup>2</sup> in this study, which corresponds to a wall temperature of approximately 950°C.

### 3.3.3. Numerical Modelling

The numerical modelling calculates the different losses of the system, assuming that the steady states is reached, and the wall temperatures are estimated according to the preliminary calculations.

#### 3.3.3.1. Radiative Losses

The surfaces of the absorber are submitted to the concentrated solar power. A part of this radiation is absorbed by the tubes and extracted by the particles, conductive losses within the tubes being negligible. But the tubes reflect the rest of the incident radiation, and emit infrared radiation. The sum of this two fluxes is named the radiosity  $J$ . As the surfaces are considered as gray body in spectral bands, the radiosities can be separated in the solar and infrared spectral bands (Eq. 11). This leads to the total radiosity of the  $i$  surface,  $J_i^{tot} = J_i^{sol} + J_i^{IR}$ . In these equations,  $F_{ij}$  is the view factor, i.e. the fraction of the flux density emitted by  $i$  and received by  $j$ . These terms are only geometric, and calculated numerically on Matlab.

$$J_i^{sol} = r_i^{sol} \left( \phi_{inc,i} + \sum_j J_j^{sol} F_{ij} \right) \quad (11.a)$$

<sup>18</sup> Le Gal A., Grange B., Tessonnaud M., Perez A., Escape C., Sans J-L., Flamant G. (2019). Thermal analysis of fluidized particle flows in a finned tube solar receiver. Solar Energy 191, pp. 19–33.

$$J_i^{IR} = \varepsilon_i^{IR} \sigma T_{wall,i}^4 + r_i^{IR} \sum_j J_j^{IR} F_{ij} \quad (11.b)$$

The radiative losses are then calculated as the total radiation which gets out of the cavity through the aperture, referred with the “0” subscript (Eq. 12).

$$\phi_{loss,rad} = \sum_j S_j F_{j0} J_j = S_0 \sum_j F_{0j} J_j \quad (12)$$

### 3.3.3.2. Convective Losses

There are two kind of convective losses in this system.

Firstly, the convective exchange inside the cavity, between active and passive surfaces and the air (Eq. 13.a). In the Clausing’s model<sup>19</sup>, the cavity is split into two zones at approximately the height level of the aperture. Above this horizontal border, the air is stagnant, its temperature is high and the convection is very low. Then, below the border, the convection is stronger because the fresh air is coming from the outside of the cavity, heated by convection and comes out of the cavity by the upper part of the aperture. Even if this phenomenon is not taking into account in this simplified model, the Clausing’s model estimates the air temperature inside the cavity by the mean temperature between the walls and the air outside the cavity,  $T_{ext}$ . Considering an outside temperature of 15°C and walls temperature of 950°C, it leads to  $T_{air}^{cav} \approx 500^\circ\text{C}$ .

Secondly, the convective exchange with the external air, at the back-face of the passive surfaces (see Figure 15). The thermal conduction through these surfaces leads to an outside wall temperature  $T_{wall}^{ext}$  higher than the external air temperature, which results in convection (Eq. 13.b).

$$\phi_{loss,conv}^{cav} = \sum_i S_i h_{air}^{cav} (T_{wall,i} - T_{air}^{cav}) \quad (13.a)$$

$$\phi_{loss,conv}^{ext} = \sum_j S_j h_{air}^{ext} (T_{wall,j} - T_{air}^{ext}) \quad (13.b)$$

A rapid estimation of external convective losses ( $\phi_{loss,conv}^{ext}$ ) indicates that they are negligible with respect to the cavity convective losses. Consequently, they are neglected. Actually, the estimation of convective losses in cavity solar receivers ( $\phi_{loss,conv}^{cav}$ ) is still a challenging subject. The convective coefficients in the two zones are thus assumed to be identical to simplify the calculation. It is taken to 10 W/m<sup>2</sup>K, value which voluntarily overestimates the convective losses. The effect of this assumption is discussed in the results section.

### 3.3.3.3. Receiver Efficiency

The power entering the solar receiver is equal to the sum of the exchanged powers (Eq. 14.a), with  $\phi_{abs}$  the power absorbed by the particles, based on their temperatures and mass flux (Eq. 14.b).

<sup>19</sup> Clausing, A.M. An analysis of convective losses from cavity solar central receivers. Sol. Energy 1981, 77, 295–300, doi:10.1016/0038-092X(81)90062-1. & Clausing, A.M. Convective losses from cavity solar receivers—Comparisons between analytical predictions and experimental results. J. Sol. Energy Eng. 1983, 105, 29–33.

$$P_{rec} = \phi_{abs} + \sum \phi_{losses} \quad (14.a)$$

$$\phi_{abs} = G_p \frac{\pi D_t^2}{4} N_t C_{p,olivine} (T_{part}^{out} - T_{part}^{in}) \quad (14.b)$$

Finally, the thermal efficiency of the receiver is the ratio between the power absorbed by the particles and the receiver power (Eq. 15). In the same way, the radiative and convective losses presented in the following section are the ratios between their corresponding power and  $P_{rec}$ , so that the sum of the losses and the efficiency is equal to 1.

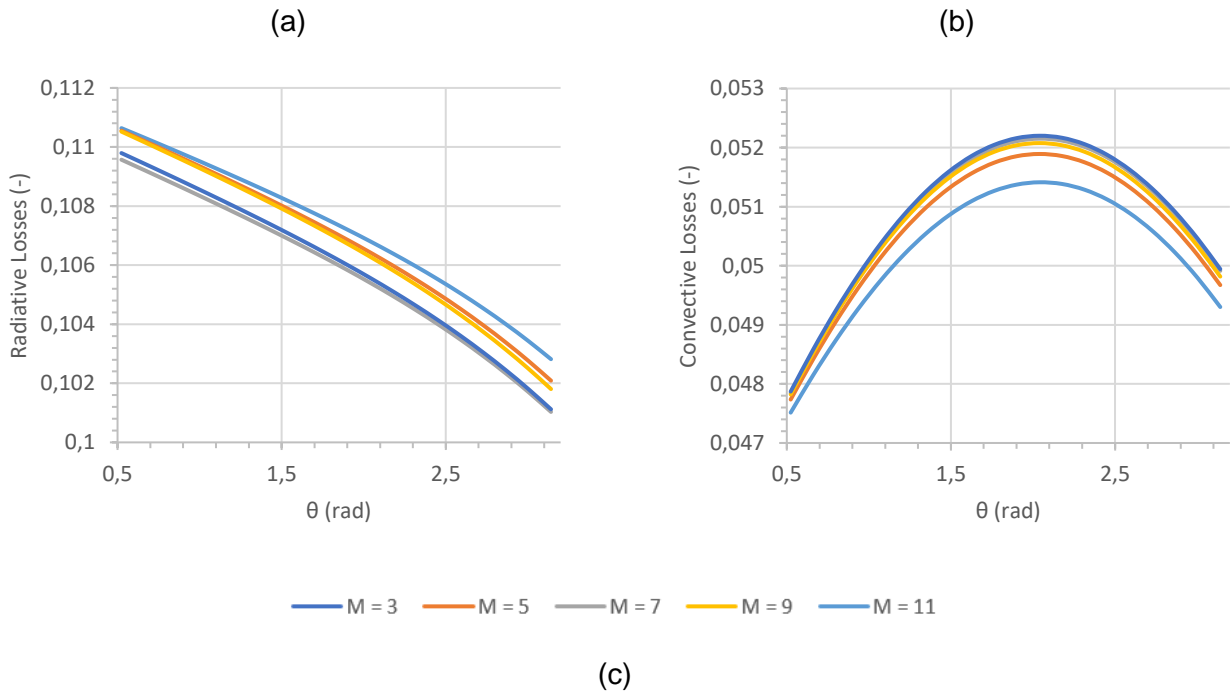
$$\eta_{rec} = \frac{\phi_{abs}}{P_{rec}} \quad (15)$$

### 3.4.Results

As mentioned previously, our goal is to study the influence of the receiver's cavity shape and geometry on its thermal performance. Even without consider a coupling with the heliostat field, the feasibility of the resulting concepts is taking into account.

#### 3.4.1. Influence of the Absorber Geometry

Both the angle  $\theta$  of the circular arc in which the absorber is inscribed (see Figure 18) and the number of tubes panels  $M$  are varied. For each value of  $\theta$ , between  $\pi/6$  and  $\pi$ , the corresponding radius of the arc is calculated from Equation 6. Figures 18.a-c show the influence of these parameters on the receiver losses and efficiency. The following parameters are fixed: the aperture of length  $L_{ape} = 4$  m and height  $H_{ape} = 5$  m is placed at a distance of the absorber  $d_{ape} = 7$  m, and is parallel to the absorber (i.e.  $\alpha = 0$ ).



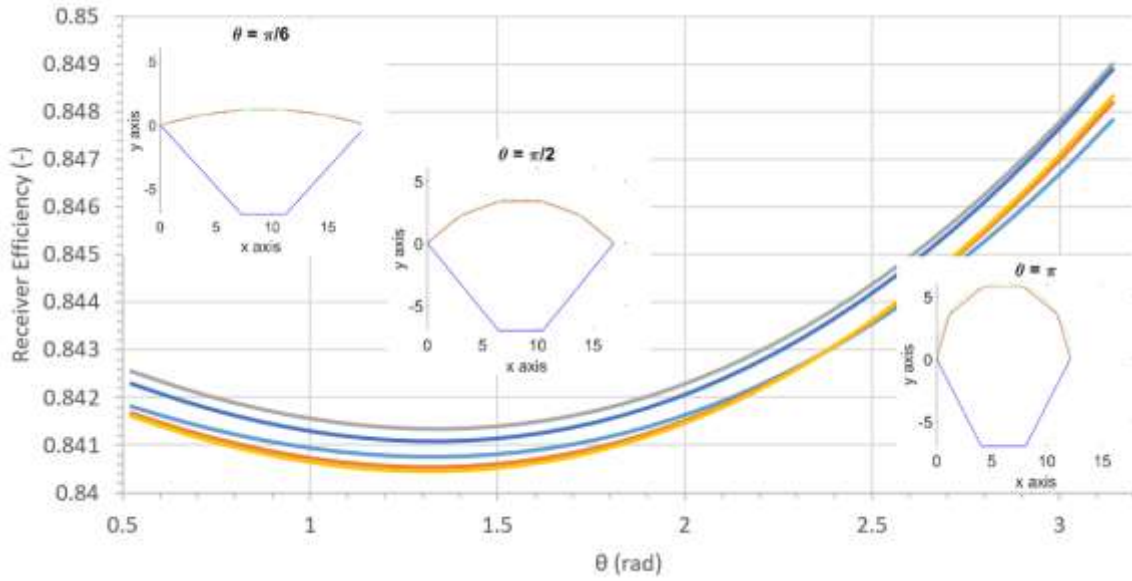


**Figure 18:** Influence of the absorber geometry on the radiative (a) and convective (b) losses, and on the receiver thermal efficiency (c).

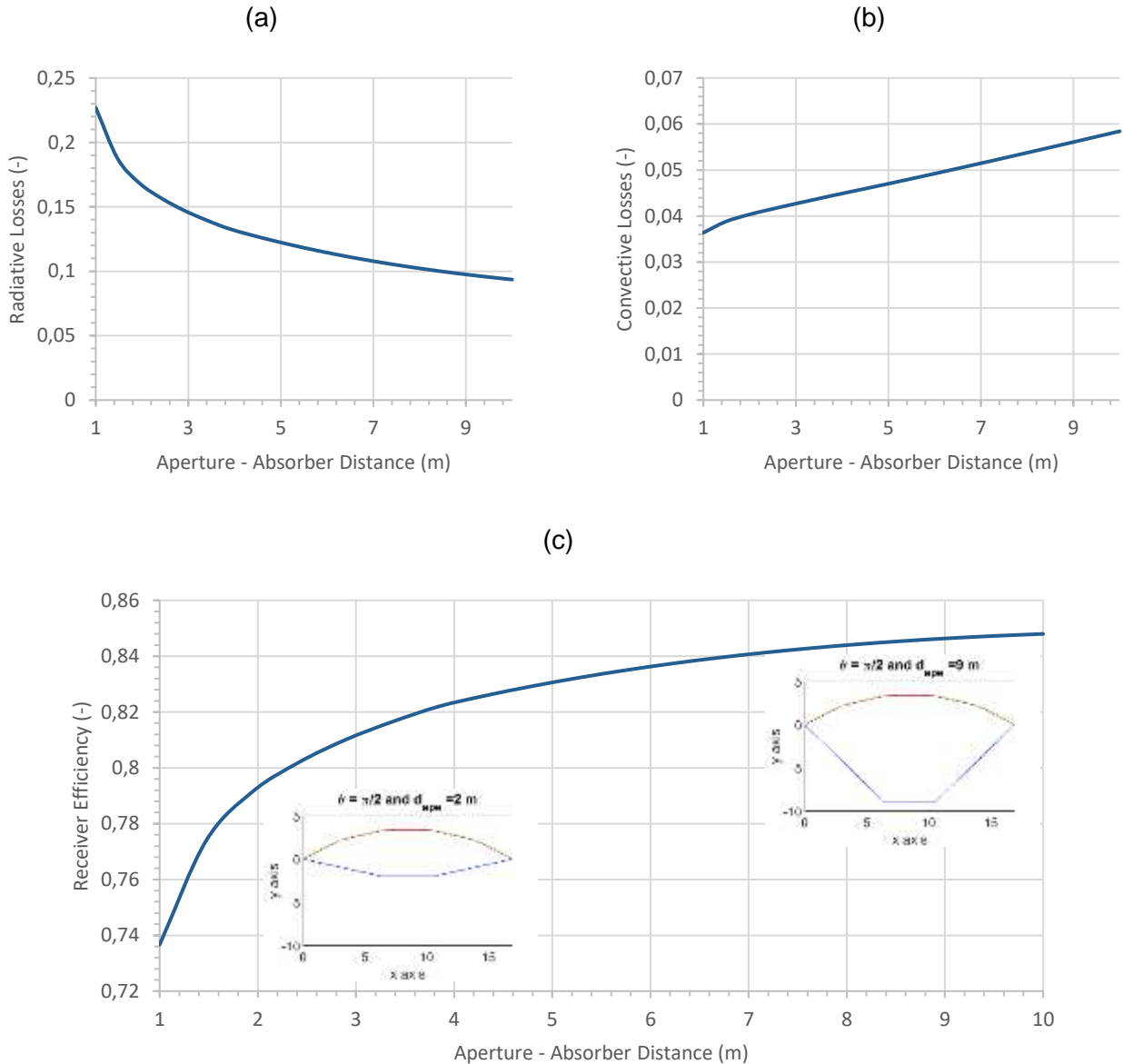
In Figure 18.c, which represents the receiver efficiency, three shapes of the receiver are presented as sub-figures, for  $\theta$  values of  $\pi/6$ ,  $\pi/2$  and  $\pi$ . The smaller the angle of the arc, the larger the radius  $r$  is to insert all the tubes in the absorber. The variations of these parameters corresponds to a distance between the two ends of the absorber between 12 m and 18.5 m.

Figure 18 indicates that the two kind of losses are influenced by the absorber geometry, but the corresponding change in the efficiency is less than 1%. The increase of the arc angle  $\theta$  results in a decrease of the distance between the two ends of the absorber, i.e. of its apparent area from the aperture, hence reducing the radiative losses. But it results in a decrease of the top and bottom passive surfaces too (with positive values of the y axis on the sub-figures), while it decreases the other top and bottom, as well as the left and right passive surfaces. Since the decrease of related areas is larger than the increase one, the convective losses decrease too, until the threshold value of  $\theta = 2\pi/3 \approx 2$  radians. After this limit, the two losses are decreasing, which results in an increase of the efficiency. According to these observations, from a simple thermal point of view, it might be reasonable to set  $\theta = \pi$ . But in practice, it will be difficult to correctly irradiate the side panels of the absorber. Furthermore, as the tubes are immersed in a dispenser fluidized bed, its dimensions have to be modified as a function of  $\theta$ . The value  $\theta = \pi$  implies to increase the size of the dispenser, and so the quantity of the particles within. For these reasons, since the influence of  $\theta$  is low on the receiver thermal efficiency, it is more realistic to set  $\theta = \pi/2$ .

The influence of the number of panels is very small. Values until  $M = 21$  have been tested, but results are not shown to not overloading the figures, because the data differs by less than 1%. Actually, increasing the number of panels results in a better fit of the absorber with the arc of circle. In practice, it is complicated to arrange a high number of tubes on too many panels. As previously, since the influence of  $M$  is low on the receiver performances, the realistic value of  $M = 5$  is set for the rest of the study.

### 3.4.2. Influence of the Aperture's Distance

The distance between the aperture and the absorber,  $d_{ape}$ , is varied between 1 and 10 m, with the same parameters as previously, an angle of the arc circle  $\theta = \pi/2$  and a number of absorber's panels  $M = 5$ . Figures 19.a-c present the changes in the losses and the thermal efficiency, with two sub-figures in Figure 19.c which show receiver shapes for values of  $d_{ape}$  of 2 and 9 m.



**Figure 19:** Influence of the aperture – absorber distance on the radiative (a) and convective (b) losses, and on the receiver thermal efficiency (c).

The distance between the aperture and the absorber has a strong effect on its thermal performance, because it affects strongly the radiative losses. Actually, increasing  $d_{ape}$  results in a decrease of the view factor between the absorber surface and the aperture, hence decreasing the radiative losses. It also slightly increases the areas of the passive surfaces, which implies a slight increase of the convective losses. Since they remain lower than the

radiative ones, the efficiency increase too. However, for the same reason as previously, it will be difficult to correctly irradiate the absorber from the heliostats with a too high value of  $d_{ape}$ . An intermediate value of  $d_{ape} = 7$  m seems to be a reasonable compromise for the following.

### 3.4.3. Influence of the Aperture inclination

The tilt angle of the aperture with respect to the vertical plane of the receiver,  $\alpha$ , varied between 0 and 45°, with the others parameters defined previously. Figures 20.a-c show the effect of the tilt angle of the aperture on the receiver performance. Two sub-figures are added showing the receiver shapes for values of  $\alpha$  of 0 and 45°.

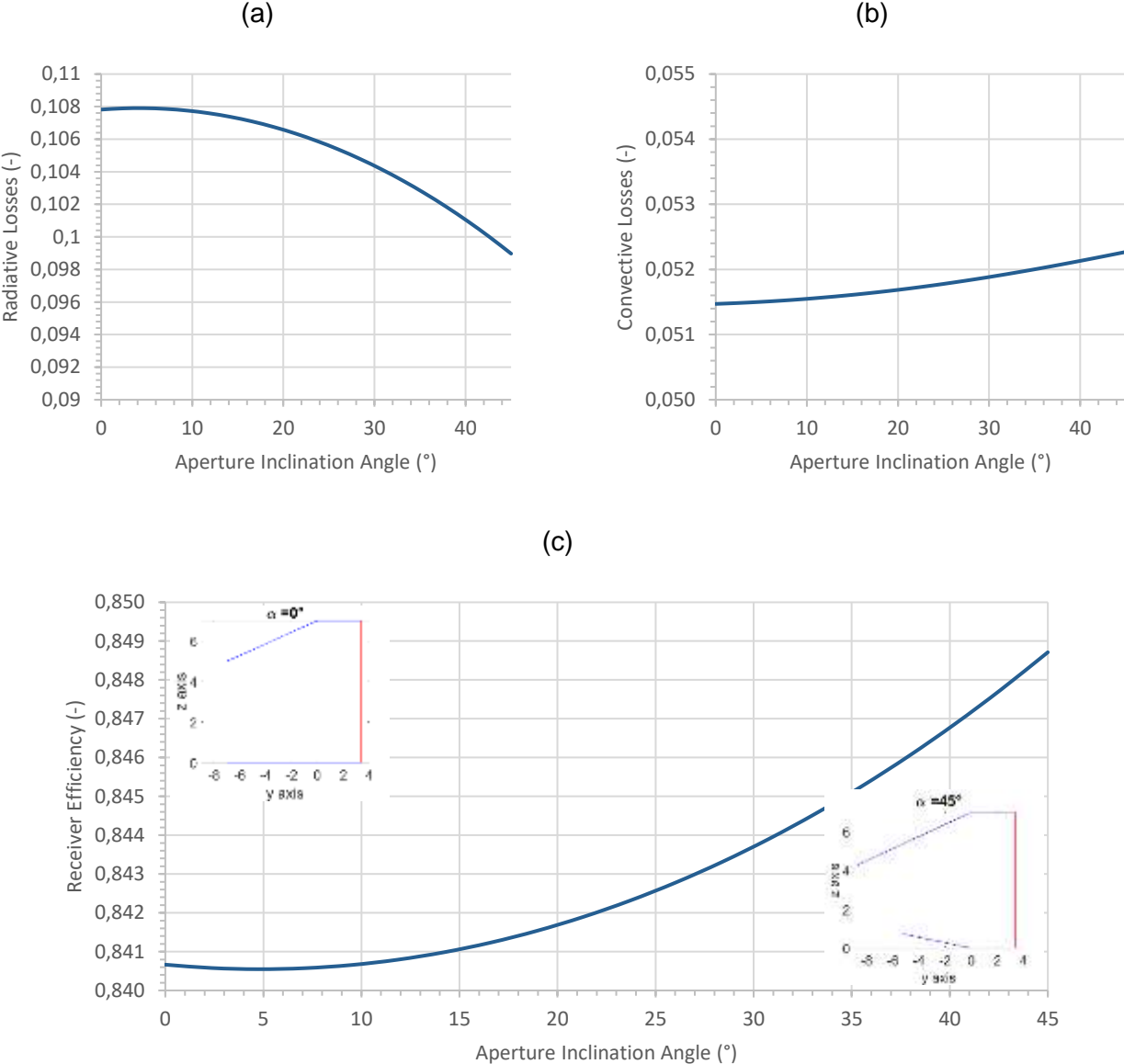


**Figure 20:** Influence of the aperture inclination on the radiative (a) and convective (b) losses, and on the receiver thermal efficiency (c).

An increase of the tilt angle of the aperture strongly decreases the apparent area of the aperture from the point of view of the absorber, hence significantly decreasing the radiative

losses, while it slightly increases the dimensions of the passive surfaces, which corresponds to a slight increase of the convective losses. Since they remain much smaller than the radiative ones, the receiver thermal efficiency is increasing with  $\alpha$ .

The optimum value of the aperture tilt angle is strongly dependent on the coupling with the heliostats field that results in a global optical and thermal efficiency. Consequently, even if a maximal tilt angle is optimal from a simple thermal point of view, it might be not optimal from the optical point of view, depending on the height of the tower and the positions of the heliostats. Based on those considerations, the intermediate value of  $\alpha = 30^\circ$  is set for the rest of the study.

3.4.4. Influence of the Aperture Dimensions

The height  $H_{ape}$  and length  $L_{ape}$  of the rectangular aperture are varied simultaneously, between 2 and 7 m both. Figure 21.a shows the evolution of the efficiency and the losses as a function of the aperture area,  $S_{ape} = H_{ape} * L_{ape}$ . The receiver efficiency is obviously maximum for the smallest aperture. Actually, increasing the dimensions of the aperture results in a slight decrease of the passive surfaces, which very slightly decreases the convective losses but they remain around 5 % for all the aperture sizes tested, while the radiative losses range from 2.31 % to 21.54 % in the same studied domain. Thus the efficiency drastically decreases, and the minimum limit of 85 % is reached for a maximum area of approximately 20 m<sup>2</sup>.

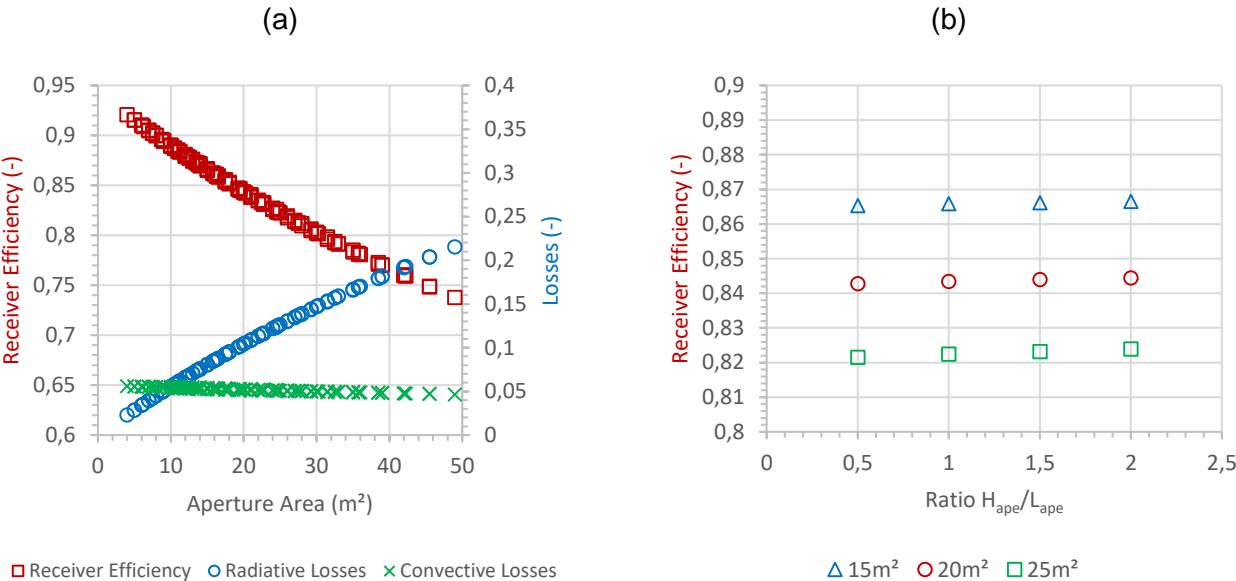


**Figure 21:** a) Influence of the aperture dimensions on the receiver performances, and b) Influence of the aperture shape on the receiver efficiency.

As the absorber is not symmetric, the influence of the height of the aperture is different of the influence of its length. Thus, Figure 21.b plots the receiver thermal efficiency as a function of the aperture shape, defined by the ratio  $H_{ape}/L_{ape}$  (square, vertical rectangle or horizontal rectangle), for three aperture areas as parameters. It indicates that from a thermal point of view, the shape of the aperture has a slight influence on the receiver efficiency, because it slightly modifies the areas of the passive surfaces and the view factor. The shape

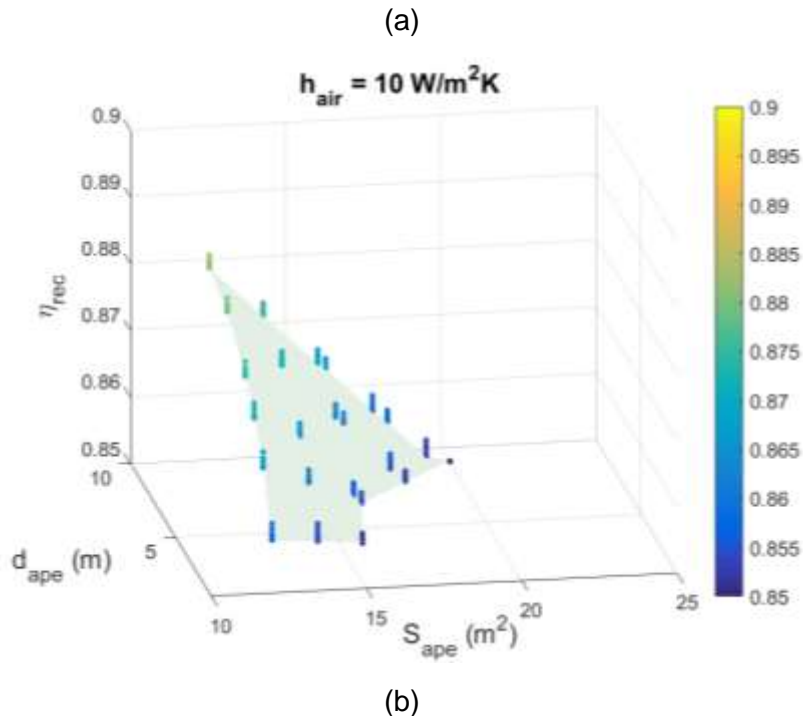
of the aperture will be more important when coupling the receiver with the heliostat field, because it affects the ability to correctly irradiate the absorber.

Due to the absorber dimensions: a height of 7 m and a distance between its two ends of 16.9 m with the parameters fixed previously, it makes more sense to choose a horizontal aperture, to easily irradiate all the tubes of the absorber.

### 3.4.5. Sensitivity Analysis

The sensitivity analysis results in the determination of the domain of parameters which allow to reach the targeted receiver efficiency of 85 %, by varying all the geometrical parameters simultaneously, and taking into account both the feasibility of the concept and the coupling with the heliostats field. This domain is shown on Figure 22.a, with an aperture tilt angle of 30°.

As mentioned above, the calculation of the convective losses is still a challenging subject. All the simulations presented in the previous section have been performed with an overall convective heat transfer coefficient of 10 W/m<sup>2</sup>K, applied on all the active and passive surfaces of the receiver, considered at a temperature of 950°C. This value of the coefficient is the maximum given by Clausen<sup>19</sup> but other considerations lead to the conclusion that convective losses have been overestimated. Firstly, the separation of the cavity in two different convective zones implies a decrease of these losses in the upper zone. Secondly, the scientific literature on high temperature solar cavity receivers indicates that the ratio of radiation to convection losses is approximately 4, whereas it is approximately 2 in our results. Consequently, the convective heat transfer coefficient was reduced to 5 W/m<sup>2</sup>K. Figure 22 illustrates the results for the two values of the convective heat transfer coefficient.



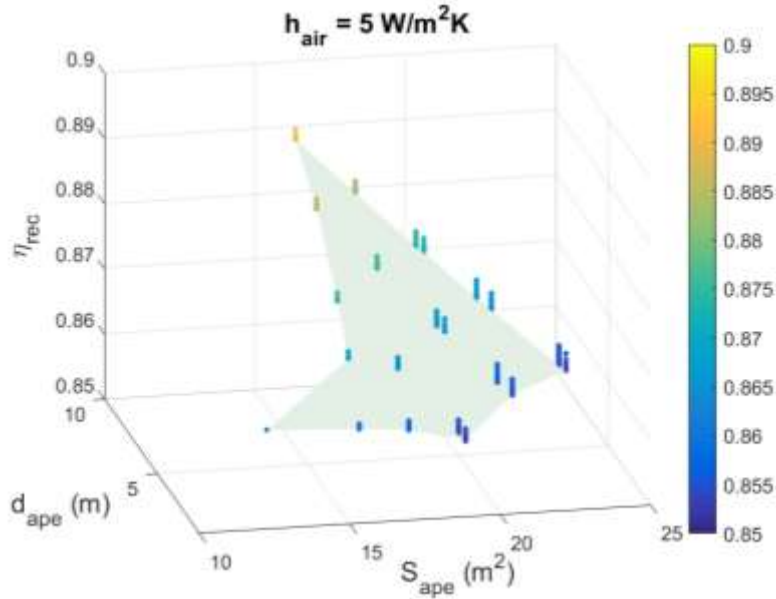


**Figure 22:** Maps of the domain of parameters that allow to reach the targeted efficiency, with an overall convection coefficient  $h_{air}$  of 10 W/m<sup>2</sup>K (a) and 5 W/m<sup>2</sup>K (b).

For  $h_{air} = 10$  W/m<sup>2</sup>K, there is no configuration leading to the targeted receiver efficiency for an aperture area larger than 20 m<sup>2</sup>. For this aperture area, the thermal efficiency reaches 85 %, and the radiative and convective losses are respectively 9.3 and 5.7 % (i.e. a ratio of 1.6). Reducing the convective losses estimation results in a significant change of this limit to an aperture area of 25 m<sup>2</sup>. Then, the radiative and convective losses are respectively 11.6 and 2.9 %, which corresponds to a ratio of 4 as expected for a high temperature cavity receiver.

### 3.5.Conclusion

This section presents a parametric study on the effect of the geometry on the thermal efficiency of a 50 MW<sub>th</sub> cavity tubular solar receiver using particles as HTF within chosen design constraints. The absorber is composed of  $M = 5$  panels to house 360 tubes (7 m height) in an arc circle of an angle  $\theta$ . According to design data, the wall temperature is 950°C for particles outlet temperature of 750°C. An either vertical or inclined aperture is used, to accommodate the main direction of the reflected solar beam by the heliostats. Various configurations are defined to reach the targeted receiver's thermal efficiency of at least 85 %. The dominant parameters that govern the receiver efficiency are the aperture area and the distance between the aperture and the absorber. In this context, the assumption on convective losses appears to be a key factor that affects the acceptable aperture surface area. For a distance between the aperture and the absorber of 9 m (and with  $\theta = 2\pi/3$ ), the efficiency threshold of 85 % is reached for aperture surface areas equal or less than 20 m<sup>2</sup> for high convection losses and it increases to 25 m<sup>2</sup> for low convection losses. In the two cases of convection losses, decreasing the distance between the aperture and the absorber decreases the aperture area that allows reaching the targeted efficiency.

#### 4. Levelized Cost of Electricity (LCOE)

This part gives an estimation of the LCOE of a 100 MW<sub>e</sub> solar power plant (baseload) using the fluidized particles in tube receiver technology.

The described plant layout was optimized for a peak load configuration in the framework of the Next-CSP H2020 project. It was adapted to a baseload configuration to fit with DOE criteria for the G3P3 comparative study.

##### 4.1. Configuration

The optimized **peak load** and not optimized **baseload** configurations are presented in Table 3 and the multi-tower layout is illustrated in Figure 23. For the baseload study, the net power is 100MW and a solar multiple of 2.5 is considered.

**Table 3.** Characteristics of the peak load and baseload configurations studied.

Peak load	Baseload
<p>150MW<sub>e</sub> – gas turbine/combined cycle (η=48,6%)            6 towers, 56.2 MW<sub>th</sub> each (net power to particles)  <i>(tower height 126m from mirror height to mid-receiver)</i>            □T<sub>particle</sub>=221°C (cold 604°C - hot 825°C)            Particle mass flowrate 220kg/s per receiver            SM=1 (peaker plant)            Horizontal conveying star configuration = 4020 m            Heat losses = 5.4% (particle handling + HX)            2 GWh<sub>th</sub> storage, 2 hot and 2 cold tanks on the floor near the power block            Yearly production = 241 GWh, Capacity factor =18.3% (Ouarzazate – Morocco, DNI 900 W/m<sup>2</sup>)</p>	<p>100MW<sub>e</sub> (2 x 50MW = 2 power blocks) – CO<sub>2</sub> supercritical cycle (η=50,2%)            Net thermal power = 100/(0.502x0.946) = 210.6 MW<sub>th</sub>            (heat transferred to particles through the receiver)            SM=2.5 → 526.5 MW<sub>th</sub>            10 towers (2 x 5 towers), 52.64 MW<sub>th</sub> each            Particle mass flowrate 199 kg/s per receiver            2 Stars configuration, horizontal conveying = 3100 m per star            14 hours storage, eq. 3 GWh<sub>th</sub>, 3 hot and 3 cold tanks on the floor  <u>Yearly production = 613.2 GWh/y, Capacity factor = 70%</u>  <i>This document gives an estimation of the CAPEX of the plant but the yearly production is not modelled. A capacity factor of 70% is considered that gives a yearly production of 613.2 GWh.</i></p>

(a)

(b)

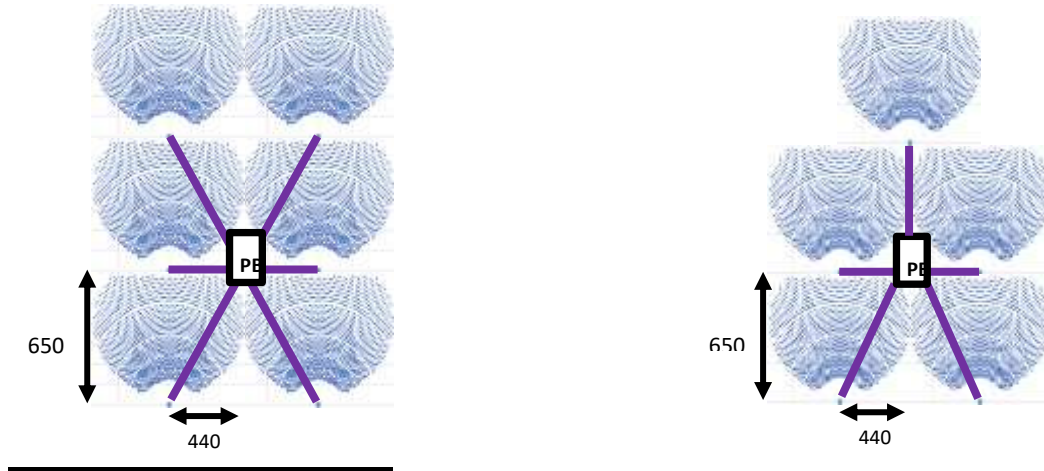


**Figure 23:** a) Peak load and b) Baseload star configurations of the solar power plants.

## 4.2. Cost Assumptions

For the cost assumption in [€], a current exchange rate of 1€ = 1.17 \$ is assumed.

### 4.2.1. Heliostats Field

The DOE requires to assume a price of 75 \$/m<sup>2</sup> per Heliostat. The mirror area to power the receiver is calculated with Equation 16.

$$A_{Heliostat} = \frac{P_{Rec}}{I * \eta_{Opti} \eta_{Ther}} \quad (16)$$

The Thermal Power  $P_{rec}$  provided to particles by a receiver is 52.64 MW<sub>th</sub> with a receiver's thermal efficiency  $\eta_{Ther}$  of 80 %. This thermal efficiency is a conservative estimation from modelling of the solar receiver<sup>20</sup>.

The annual Optical efficiency  $\eta_{Opti}$  of the solar field is 69.58 % (SBP source – Next-CSP partner). With a DNI of 950 W/m<sup>2</sup> in Dagget, US California (DOE requirement). After calculation, the area of the heliostat field is 99 551 m<sup>2</sup> per tower.

The cost for the Heliostat Field is given by Equation 17.

$$C_{Helistat Field} = 99\,551 * 75 = 7\,466\,351 \text{ \$ per tower} \quad (17)$$

As we consider 10 towers, the total cost of heliostat fields is,

$$C_{Helistat Field} = 74\,663\,510 \text{ \$}.$$

### 4.2.2. Tower

For the Tower, the following correlation from SAM is used (Eq. 18).

$$C_{tower}(SAM) = 3'000'000\$ \cdot e^{(0.0113 \cdot (h_{Tower} + H_{Heli} / 2 - H_{rec} / 2))} \quad (18)$$

<sup>20</sup> Gueguen R., Grange B., Bataille F., Mer S., Flamant G. *Shaping High Efficiency, High Temperature Cavity Tubular Solar Central Receivers*. Energies (2020) 13, 4803. doi:10.3390/en13184803.

Assuming  $h_{Tower} + h_{Heli} / 2 - h_{rec} / 2 = 126$  m,  $C_{tower} = 3\,000\,000 \times e^{(0.0113 \times (126 + 4/2 - 7.64/2))} = 12\,205\,048$  \$. Thus, for 10 towers,

$$C_{tower} = 122\,050\,482 \text{ \$}.$$

This cost is over-estimated regarding to SBP cost estimation. A cost of about 3 500 000 \$ per tower is more realistic which gives a total cost of 35 000 000 \$.

#### 4.2.3. Receiver

The receiver cost is specific to the fluidized particle in tube technology. Its design is presented in Figure 24, and its parameters are given in Table 4.

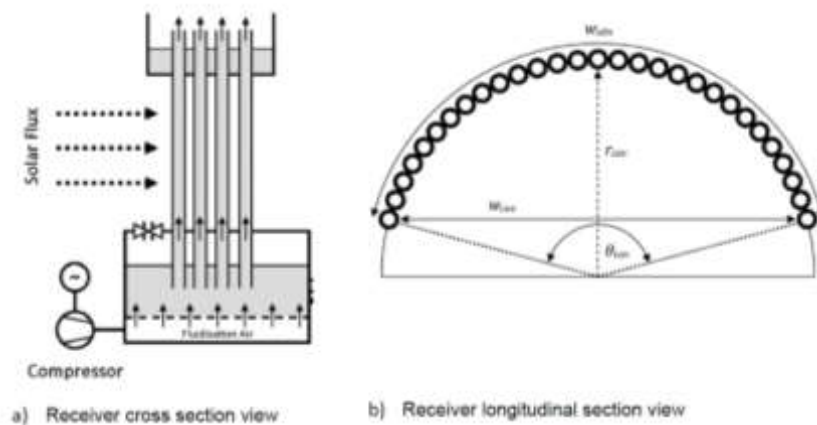


**Figure 24:** Receiver design.

**Table 4.** Receiver parameters

Parameter	Value	Units
Number of tubes	240	-
Length of tubes	7.6	m
Tube diameter	60	mm
Tube thickness	2	mm
Tube spacing	10	mm
Material	Inconel 800H	pipe
Max surface temperature	1000	°C
Cavity radius	9	m
Thermal power to be absorbed	52.64	MWth
Tube absorptivity	0.9	-
Tube emissivity	0.85	-
Average flux	500	kW/m <sup>2</sup>
Peak flux	600	kW/m <sup>2</sup>
Particles inlet temperature	580	°C
Particle outlet temperature	800	°C
Particle mass flow rate	199	Kg/s
Global heat transfer coefficient	1200	W/m <sup>2</sup> .K

The formula used to calculate the receiver cost (cf. Appendice 1) is given by equation 19.

$$C_{receiver} = C_{tube} + C_{dispenser} + C_{cavity} + C_{accessories}$$

$$With \begin{cases} C_{tube} = [nb_{tube} * (V_{inconel} * \rho_{inconel}) * C_{inconel}] + C_{pyromark} + Labour\ Cost \\ C_{dispenser} = (V_{steel} * \rho_{steel} * C_{steel}) * 1.25 \\ C_{cavity} = C_{cavity\_Next-CSP} * S_{cavity} \end{cases} \quad (19)$$

A receiver cost of 2 962 208 \$ has been calculated. Consequently, the total cost for 10 receivers is,

$$C_{receiver} = \mathbf{29\ 622\ 082\ \$}.$$
 It corresponds to a receiver cost function of 56.2\$/kW<sub>th</sub>.

#### 4.2.4. Particles Transport

To calculate the lift cost  $C_{lift}$ , a coefficient  $c_{lift}$  in [USD/(kg/s)·m] is used to estimate the price of the lift (Eq. 20). This coefficient is based on an assumption that the price is scaled linearly with lift height and mass flow rate as stated by Repole and Jeter<sup>21</sup>.

$$C_{lift} = c_{lift} \cdot \dot{m} \cdot h \quad (20)$$

Here,  $\dot{m}$  is the receiver mass flowrate at design point in kg/s.  $c$  is taken to be 58.37 [\$/((kg/s)·m)] which is based on calculation of the total cost of the development of the particle lift for 60 MW<sub>th</sub> tower that costs 523000 \$ with mass flow rate 127 kg/s of and tower height of 70 m.

The mass flowrate is calculated from the thermal power of the receiver (52.64 MW), the differential temperature (220K for supercritical CO<sub>2</sub>) and heat capacity of olivine (1200 J/kg.K). The cost of the lift is then given by Equation 21.

$$C_{lift} = 58.37 \left[ \frac{\$}{\frac{kg}{s} m} \right] * 199 \left[ \frac{kg}{s} \right] * 126 [m] = 1\ 466\ 566\ \$ \quad (21)$$

For the 10 towers, the total cost is  $C_{lift} = \mathbf{14\ 665\ 655\ \$}$ .

For the Horizontal Transport (Figure 25) from the bottom of the tower to the central power station, a conveying system with a specific configuration “in star” is considered to facilitate the transport. See plant layout in Figure 23.

<sup>21</sup> K. Repole, and M. Jeter, *Design and Analysis of a High Temperature Particulate Hoist for Proposed Particle Heating Concentrator Solar Power Systems*, Proceeding of the ASME 10<sup>th</sup> International conference on energy sustainability ES 2016, 2016.

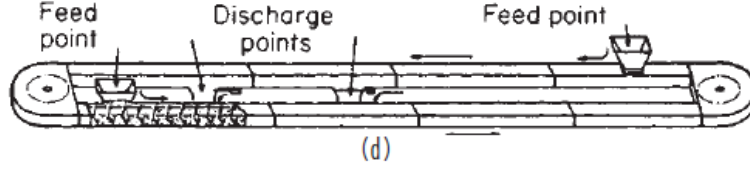


**Figure 25: Horizontal conveying system.**

The manufacture was made considering heat losses, it has been reduced to reach 5.4 % of heat Losses (discussion with manufacturer). The distance was favored by the star configuration with a total of 6.2 km between the two central power stations and towers. The capacity of each conveyors is 199 kg/s.

In the peak load LCOE study done by EDF (Partner of the Next-CSP project), the cost of the horizontal particle conveying is 31.2 M\$ for the conveyor, electric motor and inclined vibrating chutes and 3.16 M\$ for the power supply (PV farm + battery) but the total length was 8 km. By considering a total distance of 6.2 km we can estimate the total cost of horizontal conveying to

$$C_{conveyor} = 26\ 629\ 000\ \$ \text{ for the 10 towers.}$$

#### 4.2.5. Power Block

The sCO<sub>2</sub> power block is assumed as 600 \$/kW<sub>e</sub> (cost limited by DOE). This cost is excluding the primary heat exchanger. We have a power capacity of 100 MW<sub>e</sub>, the final cost of the power block is then given by Equation 22.

$$C_{Power\ Block} = 600 \left[ \frac{\$}{KW_e} \right] * 100 [MW_e] = 60\ 000\ 000\ \$ \quad (22)$$

#### 4.2.6. Heat Exchanger

##### *Suggestion 1: ANU*

The Heat Exchanger cost  $C_{HX}$  is calculated by using the formula shown in Equation 23, where  $C'_{HX}$  is the specific cost of the particle exchanger which is taken to 150 USD/KW<sub>th</sub>.

$$C_{HX} = C'_{HX} * \frac{P_{net_{Power\ Block}}}{\eta_{pb} * \eta_{part}} \quad (23)$$

The net electrical Power  $P_{net_{Power\ Block}}$  of the Power Block is 100 MW<sub>e</sub>, the efficiency of the CO<sub>2</sub> supercritical  $\eta_{pb}$  is 50.2 % . The Thermal losses  $\eta_{part}$  is a guess value of 5.4 % . The cost of the Heat Exchanger is then given by Equation 24.

$$C_{HX} = 150 \left[ \frac{\$}{KW_{th}} \right] * \frac{100[MW_e]}{0.502 * 0.946} = 31\ 586\ 129\ \$ \quad (24)$$

This cost estimation does not consider the heat transfer coefficient between particles and sCO<sub>2</sub>.

As the Next-CSP technology uses small diameter fluidized particles (~50 μm), the heat transfer coefficient is much higher than for larger particle such as the one used in the falling

particle receiver or the centrifugal rotary receiver. Therefore, the cost factor estimation is not relevant.

#### Suggestion 2: DLR

The primary heat exchanger is separated into two parts, one receiving particles at 600°C or lower, and the other part for higher temperatures. For the higher temperatures the use of more expensive nickel alloys leads to significantly increased specific cost. The following correlations are used (Eq. 25).

$$C_{HX} = \sum A_{HX} * C'_{HX}$$

$$C'_{HX} = \begin{cases} 1000 \left[ \frac{\$}{m^2} \right] & T_{in} < 600^\circ C \\ 1000 \left[ \frac{\$}{m^2} \right] + 0.3 \left[ \frac{\$}{m^2 \cdot ^\circ C^2} \right] (T_{in} - 6000[^\circ C])^2 & T_{in} > 600^\circ C \end{cases} \quad (25)$$

The temperature of the heat exchanger goes to 800°C, so the  $C'_{HX}$  for higher temperatures than 600°C is  $C'_{HX} = 1000 + 0.3 (800 - 600)^2 = 13\,000 \$/m^2$ .

The area of the heat exchanger is given by Equation 26.

$$A_{HX} = \frac{\frac{P_{elec}}{\eta_{cycle}}}{h_{HXGlobal} * \Delta T_{lm}} \quad (26)$$

Where  $h_{HXGlobal}$  is the heat exchanger global heat transfer coefficient and it can be calculated by  $1/h_{HXGLOBAL} = \frac{1}{h_{particles}} + \frac{1}{h_{sCO_2}}$ . As  $h_{particles} = 1000 \text{ W/m}^2\text{K}$  and  $h_{sCO_2} = 10000 \text{ W/m}^2\text{K}$ , it leads to  $h_{HXGlobal} = 909 \text{ W/m}^2\text{K}$ .

And the logarithmic temperature  $\Delta T_{lm}$  is giving by equation 27.

$$\Delta T_{lm} = \frac{(T_{in,particles} - T_{out,sCO_2}) - (T_{out,particles} - T_{in,sCO_2})}{\ln \left( \frac{T_{in,particles} - T_{out,sCO_2}}{T_{out,particles} - T_{in,sCO_2}} \right)} \quad (27)$$

With  $T_{in,particles} = 800^\circ C$ ,  $T_{out,particles} = 580^\circ C$ ,  $T_{out,sCO_2} = 565^\circ C$  and  $T_{in,sCO_2} = 715^\circ C$ , it leads to the logarithmic temperature  $\Delta T_{lm} = 40 \text{ K}$ . This corresponds to an area of the heat exchanger  $A_{HX} = 5740 \text{ m}^2$ .

Considering the value of the coefficient  $C'_{HX}$ , it corresponds to the heat exchanger coast (Eq. 28).

$$C_{HX} = 74\,617\,853 \$ \quad (28)$$

*Remark:* This estimation cost seems to be very high. For the LCOE calculation, we will use the ANU estimation cost even if it does not take into account the heat transfer coefficient.

#### 4.2.7. Storage

The DOE requires a storage of 14 hours. The associated energy is then calculated (Eq. 29).

$$P_{storage} = hours * \frac{P_{net_{Power\ Block}}}{\eta_{pb} * \eta_{HX}} \quad (29.a)$$

$$P_{storage} = 14 * \frac{100}{0.502 * 0.946} = 2.95 \text{ GWh}_{th} \quad (29.b)$$

It corresponds to a particle mass of 40 201 tons of olivine:  $m_{storage} = P_{storage} * \frac{3600}{C_{p,olivine}} * \Delta T$ .

Three cold tanks and three hot tanks are necessary for a such thermal storage. An estimation from Smulder – Eiffage (possible supplier) gives a cost of 14 040 000 \$ for the 6 tanks. The price of olivine is about 175 \$/ton. So the particle cost will be 40 201 \* 175 = 7 035 092 \$. The cost of the storage system is then calculated by adding the results of previous values (Eq. 30).

$$C_{storage} = 14\,040\,000 + 7\,035\,092 = \mathbf{21\,075\,092\ \$} \quad (30)$$

The balance of plant is included in the cost calculation of the system storage; it represents the cost of the construction and field preparation and the related cost is given by the DOE,  $C_{balance\ of\ plant} = 0.102 * P_{el} = \mathbf{10\,200\,000\ \$}$ .

#### 4.3.LCOE Calculation

The correlation for the LCOE calculation is given by Equation 31.

$$LCOE = \frac{C_{total} \cdot CRF + OM_{fix} \cdot P_{el}}{E_{el,net}} + OM_{var} \quad (31)$$

Where  $C_{total}$  (Eq. 32.a) is the sum of the direct (Eq. 32.b) and indirect (Eq. 32.c) costs that can be calculated from the contingency factor, the construction factor and the capital cost (Eq. 32.d). All these values are given by the DOE (Table 5).

$$C_{total} = C_{direct} + C_{indirect} \quad (32.a)$$

$$C_{direct} = (1 + f_{contingency}) \cdot C_{cap} \quad (32.b)$$

$$C_{indirect} = f_{construction} \cdot C_{direct} + C_{land} \quad (32.c)$$

$$C_{cap} = C_{field} + C_{rec} + C_{tower} + C_{part\_lift} + C_{part\_transport} + C_{storage} + C_{HX} + C_{cycle} + C_{BOP} \quad (32.d)$$

Then, the Capacity Recovery factor (CRF) is given by Equation 33.a. It depends on the real discount factor  $f'$  (Eq. 33.b).

Each value of the previous formulas and other values such as the cost of land, annual fixed operation and maintenance cost, variable operation and maintenance cost, site preparation are in the Table 5.

$$CRF = \frac{f' \cdot (1 + f')^N}{(1 + f')^N - 1} \quad (33.a)$$

$$f' = \frac{(1 + f)}{(1 + i)} - 1 \quad (33.b)$$

**Table 5.** Useful variables for LCOE calculation

f':( %)	0,024
f: Discount rate (%)	0,050
i: inflation rate (DOE)(%)	0,025
N: lifetime (years)	30
CRF:	0,047
Cost escalation rate (%)	2,5
Contingency (%)	0,1
EPC(engineer-procure-construct)/Owner Cost (%)	9
Land cost ( /m2)	2,130
Land Cost (\$)	12 183 600
Taxes (Federal) (%)	35
Taxes (State) (%)	5
Insurance (%)	-
Salvage rate (%)	-
Financed (%)	50
Construction (%)	0,10
Annual fixed Operation and maintenance cost (\$/Kwe)	40
Variable Operation and maintenance cost (\$/KWh)	0,003
Site preparation (\$/KWh)	10

The elements for the capital cost calculation are presented in Table 6. The distribution of the different costs is presented in Figure 26.

**Table 6.** Component costs for capital cost calculation

<b>COST</b>		
<b>C<sub>tower</sub></b>	<b>122 050 482</b>	<b>\$</b>
<b>C<sub>heliostat field</sub></b>	<b>74 663 510</b>	<b>\$</b>
<b>C<sub>receiver</sub> <i>Next-CSP estimation</i></b>	<b>29 622 082</b>	<b>\$</b>
<b>C<sub>particles transport</sub></b>	<b>41 294 655</b>	<b>\$</b>
<b>C<sub>power block</sub> <i>sCO<sub>2</sub> cycle</i></b>	<b>60 000 000</b>	<b>\$</b>
<b>C<sub>heat exchanger</sub> <i>ANU calculation</i></b>	<b>31 586 129</b>	<b>\$</b>
<b>C<sub>storage</sub></b>	<b>21 075 092</b>	<b>\$</b>
<b>C<sub>balance of plant</sub></b>	<b>10 200 000</b>	<b>\$</b>

$$C_{cap} = C_{field} + C_{rec} + C_{tower} + C_{part\_lift} + C_{part\_transport} + C_{storage} + C_{HX} + C_{cycle} + C_{BOP}$$

$$= 390\,491\,951 \text{ \$}$$

$$C_{direct} = (1 + f_{contingency}) \cdot C_{cap} = (1+0.1) \cdot 390\,491\,951 = 429\,541\,146 \text{ \$}$$

$$C_{indirect} = f_{construction} \cdot C_{direct} + C_{land} = 0.1 \cdot 429\,541\,146 + (2.130 \cdot 5\,720\,000 \text{m}^2) = 55\,137\,714 \text{ \$}$$

$$C_{total} = C_{direct} + C_{indirect} = 429\,541\,146 + 55\,137\,714 = 484\,678\,860 \text{ \$}$$

$$CRF = 0.047$$

$$OM_{fix} = 40$$

$$OM_{var} = 0.003$$

$$PeI = 100\,000$$

$$E_{el,net} = 613\,200\,000 \text{ (not calculated)}$$

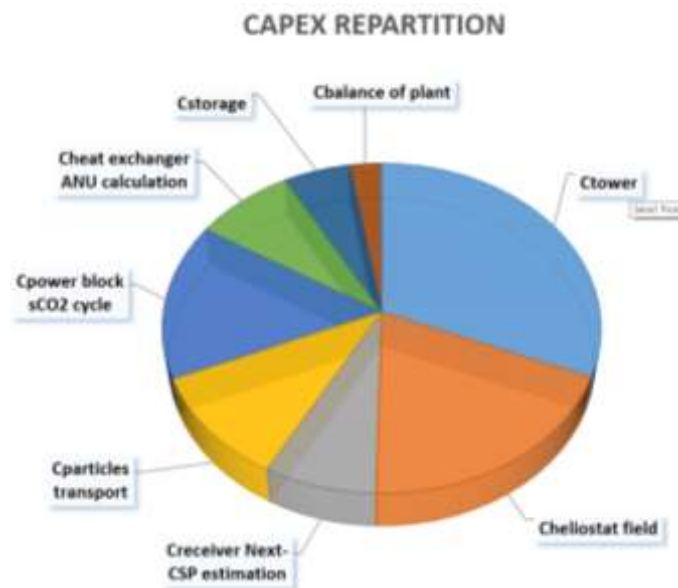


**Figure 26:** Distribution of the costs of the solar power plant.

This finally leads to the LCOE calculation, where the details are given in Equation 34.

$$LCOE = \frac{557\,633\,509 \cdot 0.047 + 40 \cdot 100\,000}{613\,200\,000} + 0.003 = 0.0467 \text{ \$/kWh}_e \quad (34)$$

Except the receiver technology, the main difference of the CNRS technology with respect to SNL and DLR technologies is the particle size and cost. The use of small particles allows the integration of fluidized bed heat exchangers in the conversion loop that results in higher wall-to-particle heat transfer than heat exchanger solutions adapted to large particles. Consequently, the heat exchange surface area (and cost) is lower for the same exchanged power.

The presented LCOE calculation is an estimation as the solar multiple and the capacity factor are assumptions and have not been calculated. An annual simulation of the plant production is necessary to improve these data.

Remark:

The tower cost calculated using SAM correlation represents about 31 % of the total investment cost. That is huge and not realistic. By using the SBP (project partner) estimation cost of 3 500 000 \$/tower, it leads to another capital cost (Eq. 35.a) and then to another LCOE value (Eq. 35.b), as shown in Figure 27.

$$C_{\text{cap}} = 303\,441\,468 \$ \quad (35.a)$$

$$\text{LCOE} = 0.0386 \$/kWe \quad (35.b)$$

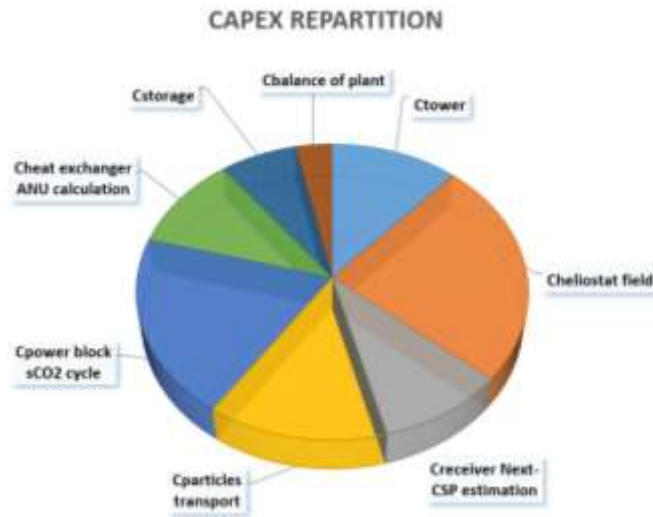


**Figure 27:** Repartition of the costs with the BSP estimation.

## 5. Conclusion

The fluidized particle-in-tube technology proves its ability to accept high values of particle mass flow rates; 0.54 kg/s is demonstrated that is twice the expected objective. Particle flow along the tube exhibits strong changes, in particular the axisymmetric slugging regime is detected at approximately 1.7 m above the secondary air injection. Fortunately, this transition is very sensitive to the operation temperature. It shifts upward with an increase of particle flow temperature. Moreover, the effect of the temperature and pressure variation along the tube is propitious for the transition to the “turbulent” fluidization regime that is favorable to wall-to-fluidized bed heat transfer.

The scaling-up of the technology to very long tube (> 10m) seems not realistic due to the previous considerations. Consequently, we assumed that 7-8 m long tubes are acceptable for a commercial-scale solar receiver. The proposed model of a 50 MW<sub>th</sub> solar receiver indicates that a thermal efficiency of 90% is feasible but the size of the cavity aperture is too small to allow a high value of the optical efficiency (spillage losses). Nevertheless, 85% thermal efficiency is a realistic target.

LCOE estimation indicates that the objective of c\$5/kWh is attainable with the fluidized particle-in-tube technology. However, a more detailed performance evaluation including a yearly production calculation is necessary to confirm the data.

## Appendix 1: Excel sheet for Receiver cost calculation

### Receiver cost function

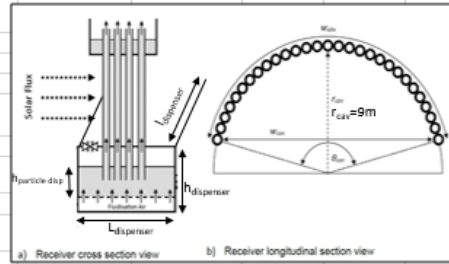
$$P_{th} = 52,6 \text{ MW}_{th}$$

variable to define by user

$$C_{receiver} = C_{tube} + C_{dispenser} + C_{cavity} + C_{accessories}$$

$$C_{receiver} = 2\,962\,208 \text{ \$ for a 52,6 MWth receiver}$$

$$C_{receiver} = 29\,622\,082 \text{ \$ for a 526 MWth power plant}$$



### C<sub>tube</sub>

$$C_{tube} = [n_{tube} \times (V_{inconel} \cdot \rho_{inconel}) \times C_{inconel}] + C_{pyromark} + \text{Labour Cost}$$

$V_{inconel} = \pi \cdot (h_{tube} + 1) \cdot (r_{out}^2 - r_{in}^2) + V_{finz}$	$n_{tube} = 240$
$V_{inconel} = 4,35E-03 \text{ m}^3/\text{tube}$	$r_{out} = 0,03$
	$r_{in} = 0,028$
$C_{pyromark} = A_{tube} \cdot LCDC \cdot n_{tube}$	$h_{tube} = 7,64 \text{ m}$
$C_{pyromark} = 99187 \text{ \$}$	$\rho_{inconel} = 8191 \text{ kg/m}^3$
	$C_{inconel} = 140 \text{ \$/kg}$
Labour cost $n_{tube} \times n_{hour\ per\ tube} \times \text{hourly cost}$	$LCDC_{pyromark2500} = 287 \text{ \$/m}^2$
Labour cost = 1344000	
$C_{tube} = 2\,639\,946 \text{ \$}$	

The receiver mass is given by  $m_{receiver} = m_{tube} + m_{dispenser} + m_{particle}$

$$m_{receiver} = 82,8 \text{ tons}$$

### C<sub>pyromark</sub> Whittaker

$A_{tube} = 1,43993746 \text{ m}^2/\text{tube}$
$C_{pyromark} = 85 \text{ \$/L}$
$S_{pyromark} = 8,18 \text{ m}^2/\text{L}$
$C_{pyromark} = [(n_{tube} \times A_{tube} \times 2) / S_{pyromark}] \times C_{pyromark}$
$C_{pyromark} = 7182 \text{ \$}$

### C<sub>dispenser</sub>

$$C_{dispenser} = (V_{steel} \cdot \rho_{steel} \cdot C_{steel}) \times 1,25$$

$\Delta T_{particle} = 220 \text{ K}$	
$m_{particle} = P_{th} / (C_{p,air} \cdot \Delta T)$	$C_{p,air} = 1200 \text{ J/kg.K}$
$m_{particle} = 199 \text{ kg/s}$	$\rho_{air} = 3400 \text{ kg/m}^3$
	$\rho_{fluidized\ bed} = 1190 \text{ kg/m}^3$
$V_{particle\ dispenser} = m_{buffer} / \rho_{fluidized\ bed}$	$r_{cavity} = 9 \text{ m}$
$V_{particle\ dispenser} = 50,3 \text{ m}^3$	$L_{dispenser} = 18 \text{ m}$
	$l_{dispenser} = 9 \text{ m}$
$h_{particle\ dispenser} = V_{particle\ dispenser} / (L_{dispenser} \cdot l_{dispenser})$	$t_{buffer} = 300 \text{ second}$
$h_{particle\ dispenser} = 0,31 \text{ m}$	$m_{buffer} = 59822,21 \text{ kg}$

To set the height of the dispenser we consider the fluidized bed height and we add 25cm for the sky above and 10cm for the fluidization air injection below.

$$h_{dispenser} = 0,66 \text{ m}$$

$$A_{dispenser} = 2 \cdot (L_{dispenser} \cdot l_{dispenser}) + 2 \cdot (L_{dispenser} \cdot h_{dispenser}) + 2 \cdot (l_{dispenser} \cdot h_{dispenser})$$

$$A_{dispenser} = 359,7 \text{ m}^2$$

The steel thickness is arbitrary set to 5mm

$$V_{steel} = 1,80 \text{ m}^3$$

$$\rho_{steel} = 8000 \text{ kg/m}^3$$

$$C_{steel} = 5,00 \text{ \$/kg}$$

$$C_{dispenser} = 89\,914 \text{ \$}$$